Arts & Sciences Articles

Arts and Sciences

Target and beam-target spin asymmetries in exclusive pi(+) and pi(-) electroproduction with 1.6-to 5.7-GeV electrons

P. E. Bosted
bosted@jlab.org

A. S. Biselli

S. Careccia

G. Dodge

R. Fersch

See next page for additional authors

Authors

P. E. Bosted, A. S. Biselli, S. Careccia, G. Dodge, R. Fersch, N. Guler, S. E. Kuhn, J. Pierce, Y. Prok, X. Zheng, K. P. Adhikari, D. Adikaram, Z. Akbar, M. J. Amaryan, S. Anefalos Pereira, G. Asryan, H. Avakian, R. A. Badui, J. Ball, N. A. Baltzell, M. Battaglieri, V. Batourine, I. Bedlinskiy, S. Boiarinov, and Keith A. Griffioen

Target and beam-target spin asymmetries in exclusive π^+ and π^- electroproduction with 1.6- to 5.7-GeV electrons

P. E. Bosted,[40,*] A. S. Biselli,[9] S. Careccia,[28] G. Dodge,[28] R. Fersch,[7] N. Guler,[28,†] S. E. Kuhn,[28] J. Pierce,[34] Y. Prok,[28] X. Zheng,[39] K. P. Adhikari,[24] D. Adikaram,[28,‡] Z. Akbar,[11] M. J. Amaryan,[28] S. Anefalos Pereira,[16] G. Asryan,[41] H. Avakian,[34] R. A. Badui,[10] J. Ball,[6] N. A. Baltzell,[1,‡] M. Battaglieri,[17] V. Batourine,[34] I. Bedlinskiy,[21] S. Boiarinov,[34] W. J. Briscoe,[13] S. Bültmann,[28] V. D. Burkert,[34] T. Cao,[32] D. S. Carman,[34] A. Celentano,[17] S. Chandavar,[27] G. Charles,[20] T. Chetry,[27] G. Ciullo,[15] L. Clark,[37] L. Colaneri,[18,30] P. L. Cole,[14] M. Contalbrigo,[15] O. Cortes,[14] V. Crede,[11] A. D'Angelo,[18,30] N. Dashyan,[41] R. De Vita,[17] A. Deur,[34] C. Djalali,[32] R. Dupre,[20] H. Egiyan,[34] A. El Alaoui,[35,1] L. El Fassi,[24] P. Eugenio,[11] E. Fanchini,[17] G. Fedotov,[32,31] A. Filippi,[19] J. A. Fleming,[36] T. A. Forest,[14] A. Fradi,[20] M. Garçon,[6] N. Gevorgyan,[41] Y. Ghandilyan,[41] G. P. Gilfoyle,[29] K. L. Giovanetti,[22] F. X. Girod,[34] C. Gleason,[32] W. Gohn,[8,§] E. Golovatch,[31] R.W. Gothe,[32] K. A. Griffioen,[40] L. Guo,[10,34] K. Hafidi,[1] C. Hanretty,[39,‡] N. Harrison,[8,‡] M. Hattawy,[1,‖] D. Heddle,[7,34] K. Hicks,[27] M. Holtrop,[25] S. M. Hughes,[36] Y. Ilieva,[32] D. G. Ireland,[37] B. S. Ishkhanov,[31] E. L. Isupov,[31] D. Jenkins,[38] H. Jiang,[32] H. S. Jo,[20] K. Joo,[8] S. Joosten,[33] D. Keller,[39] M. Khandaker,[14] W. Kim,[23] A. Klein,[28] F. J. Klein,[5] V. Kubarovsky,[34] S. V. Kuleshov,[35,21] L. Lanza,[18] P. Lenisa,[15] K. Livingston,[37] H. Y. Lu,[32] I. J. D. MacGregor,[37] N. Markov,[8] M. E. McCracken,[4] B. McKinnon,[37] C. A. Meyer,[4] R. Minehart,[39] M. Mirazita,[16] V. Mokeev,[34] A. Movsisyan,[15] E. Munevar,[34] C. Munoz Camacho,[20] P. Nadel-Turonski,[34] L. A. Net,[32] A. Ni,[23] S. Niccolai,[20] G. Niculescu,[22] I. Niculescu,[22] M. Osipenko,[17] A. I. Ostrovidov,[11] R. Paremuzyan,[25] K. Park,[34] E. Pasyuk,[34] P. Peng,[39] W. Phelps,[10] S. Pisano,[16] O. Pogorelko,[21] J. W. Price,[2] S. Procureur,[6] D. Protopopescu,[25,¶] A. J. R. Puckett,[8] B. A. Raue,[10,34] M. Ripani,[17] A. Rizzo,[18,30] G. Rosner,[37] P. Rossi,[34,16] P. Roy,[11] F. Sabatié,[6] C. Salgado,[26] R. A. Schumacher,[4] E. Seder,[8] Y. G. Sharabian,[34] A. Simonyan,[41] Iu. Skorodumina,[32,31] G. D. Smith,[36] N. Sparveris,[33] Ivana Stankovic,[36] S. Stepanyan,[34,7] I. I. Strakovsky,[13] S. Strauch,[32] V. Sytnik,[35] M. Taiuti,[12,#] Ye Tian,[32] B. Torayev,[28] M. Ungaro,[34] H. Voskanyan,[41] E. Voutier,[20] N. K. Walford,[5] D. P. Watts,[36] X. Wei,[34] L. B. Weinstein,[28] M. H. Wood,[3] N. Zachariou,[36] L. Zana,[36,25] J. Zhang,[34] Z. W. Zhao,[28,34] and I. Zonta[18,30]

(CLAS Collaboration)

[1]*Argonne National Laboratory, Argonne, Illinois 60439, USA*
[2]*California State University, Dominguez Hills, Carson, California 90747, USA*
[3]*Canisius College, Buffalo, New York 14208, USA*
[4]*Carnegie Mellon University, Pittsburgh, Pennsylvania 15213, USA*
[5]*Catholic University of America, Washington, DC 20064, USA*
[6]*CEA, Centre de Saclay, Irfu/Service de Physique Nucléaire, F-91191 Gif-sur-Yvette, France*
[7]*Christopher Newport University, Newport News, Virginia 23606, USA*
[8]*University of Connecticut, Storrs, Connecticut 06269, USA*
[9]*Fairfield University, Fairfield, Connecticut 06824, USA*
[10]*Florida International University, Miami, Florida 33199, USA*
[11]*Florida State University, Tallahassee, Florida 32306, USA*
[12]*Università di Genova, I-16146 Genova, Italy*
[13]*The George Washington University, Washington, DC 20052, USA*
[14]*Idaho State University, Pocatello, Idaho 83209, USA*
[15]*INFN, Sezione di Ferrara, I-44100 Ferrara, Italy*
[16]*INFN, Laboratori Nazionali di Frascati, I-00044 Frascati, Italy*
[17]*INFN, Sezione di Genova, I-16146 Genova, Italy*
[18]*INFN, Sezione di Roma Tor Vergata, I-00133 Rome, Italy*
[19]*INFN, Sezione di Torino, I-10125 Torino, Italy*
[20]*Institut de Physique Nucléaire, CNRS/IN2P3 and Université Paris Sud, F-91405 Orsay, France*
[21]*Institute of Theoretical and Experimental Physics, Moscow, 117259, Russia*
[22]*James Madison University, Harrisonburg, Virginia 22807, USA*
[23]*Kyungpook National University, Daegu 41566, Republic of Korea*
[24]*Mississippi State University, Mississippi State, Mississippi 39762-5167, USA*
[25]*University of New Hampshire, Durham, New Hampshire 03824-3568, USA*
[26]*Norfolk State University, Norfolk, Virginia 23504, USA*
[27]*Ohio University, Athens, Ohio 45701, USA*
[28]*Old Dominion University, Norfolk, Virginia 23529, USA*
[29]*University of Richmond, Richmond, Virginia 23173, USA*
[30]*Universita' di Roma Tor Vergata, I-00133 Rome Italy*
[31]*Skobeltsyn Institute of Nuclear Physics, Lomonosov Moscow State University, 119234 Moscow, Russia*
[32]*University of South Carolina, Columbia, South Carolina 29208, USA*
[33]*Temple University, Philadelphia, Pennsylvania 19122, USA*
[34]*Thomas Jefferson National Accelerator Facility, Newport News, Virginia 23606, USA*

^{35}*Universidad Técnica Federico Santa María, Casilla 110-V Valparaíso, Chile*
^{36}*Edinburgh University, Edinburgh EH9 3JZ, United Kingdom*
^{37}*University of Glasgow, Glasgow G12 8QQ, United Kingdom*
^{38}*Virginia Tech, Blacksburg, Virginia 24061-0435, USA*
^{39}*University of Virginia, Charlottesville, Virginia 22901, USA*
^{40}*College of William and Mary, Williamsburg, Virginia 23187-8795, USA*
^{41}*Yerevan Physics Institute, 375036 Yerevan, Armenia*

Beam-target double-spin asymmetries and target single-spin asymmetries in exclusive π^+ and quasiexclusive π^- electroproduction were obtained from scattering of 1.6- to 5.7-GeV longitudinally polarized electrons from longitudinally polarized protons (for π^+) and deuterons (for π^-) using the CEBAF Large Acceptance Spectrometer (CLAS) at Jefferson Lab. The kinematic range covered is $1.1 < W < 2.6$ GeV and $0.05 < Q^2 < 5$ GeV^2, with good angular coverage in the forward hemisphere. The asymmetry results were divided into approximately 40 000 kinematic bins for π^+ from free protons and 15 000 bins for π^- production from bound nucleons in the deuteron. The present results are found to be in reasonable agreement with fits to previous world data for $W < 1.7$ GeV and $Q^2 < 0.5$ GeV^2, with discrepancies increasing at higher values of Q^2, especially for $W > 1.5$ GeV. Very large target-spin asymmetries are observed for $W > 1.6$ GeV. When combined with cross-section measurements, the present results can provide powerful constraints on nucleon resonance amplitudes at moderate and large values of Q^2, for resonances with masses as high as 2.3 GeV.

I. INTRODUCTION

Exclusive electroproduction of pseudoscalar mesons is a process that is sensitive to the detailed internal structure of the nucleon. The process is particularly sensitive to contributions from individual nucleon resonance states. Photoproduction and very low Q^2 electroproduction continue to provide insight into the static properties of the resonances, such as mass, width, parity, spin, and decay branching ratios. Larger values of Q^2 are needed to study transition form factors, and also reveal the existence of resonances that are suppressed in photoproduction. Initial large-Q^2 measurements of spin-averaged cross sections for exclusive π^+ electroproduction from Cornell [1,2] had limited statistical accuracy. Recent measurements from Jefferson Lab (JLab) [3–8] have greatly improved the situation. A relatively limited data set exists for exclusive π^- electroproduction (including Refs. [1,2,9,10]).

The use of polarized nucleon targets and polarized electron beams is particularly useful in distinguishing between resonances of different spin, isospin, and parity, because all single-spin asymmetries vanish in the absence of interference terms. Beam asymmetries at large Q^2 were published from JLab for $W < 1.7$ GeV [6] and are also the subject of an early investigation for $W > 2$ GeV [11]. Beam-target asymmetries

for positive pions were reported from a pilot experiment at Jefferson Lab [12].

The present experiment provides the first body of high-statistical precision target and beam-target asymmetries spanning a wide range of Q^2 and W, for both π^+ and π^- electroproduction. The π^+ results are complementary to results from two other Jefferson Lab experiments, named eg4 [13] and eg1-dvcs [14], focused on the low Q^2 and high Q^2 regions, respectively.

After a summary of the formalism, details of the experimental setup, analysis, and results are presented in the following sections.

II. FORMALISM

Because both the beam and the target were longitudinally polarized, we could, in principle, extract three spin asymmetries, defined by

$$\sigma = \sigma_0(1 + P_B A_{LU} + P_T A_{UL} + P_B P_T A_{LL}), \qquad (1)$$

where P_B and P_T are the longitudinal beam and target polarizations, respectively, σ_0 is the spin-averaged cross section, and A_{LU}, A_{UL}, and A_{LL} are the beam, target, and beam-target asymmetries, respectively. The cross sections and asymmetries are all functions of five independent variables. For this analysis, the variables $[W, Q^2, \cos(\theta^*), \phi^*, \epsilon]$ are used, where θ^*, ϕ^* are the center-of-mass decay angles of the final state with invariant mass W into a meson and a nucleon, Q^2 is the squared virtual photon four-momentum, and ϵ is the virtual photon polarization. The bins in ϵ have a one-to-one correlation with the different beam energies of the experiment. We use the convention that the center-of-mass final state decay polar angle $\theta^* = 0$ degrees corresponds to a forward-going meson. The definition of ϕ^* is the opening angle between $(\vec{q} \times \vec{e})$ and $(\vec{q} \times \vec{p}_\pi)$, where $\vec{e}$ is the incident electron

---
*bosted@jlab.org

†Present address: Spectral Sciences Inc., Burlington, MA 01803.

‡Present address: Thomas Jefferson National Accelerator Facility, Newport News, Virginia 23606.

§Present address: University of Kentucky, Lexington, KY 40506.

$^\|$Present address: Institut de Physique Nucléaire, CNRS/IN2P3 and Université Paris Sud, Orsay, France.

¶Present address: University of Glasgow, Glasgow G12 8QQ, United Kingdom.

$^\#$Present address: INFN, Sezione di Genova, 16146 Genova, Italy.

TABLE I. Composition of the three targets used in this analysis, in units of g/cm^2 as a function of the total length of the target L (range 1.8–2.2 cm) and effective ammonia length l_A (range 0.53–0.73 cm).

Target	NH$_3$	ND$_3$	He	Al	C
NH$_3$	0.917l_A	–	0.145$(L - l_A)$	0.09	–
ND$_3$	–	1.056l_A	0.145$(L - l_A)$	0.09	–
Carbon	–	–	0.145$(L - 0.23)$	0.09	0.499

momentum, $\vec{q}$ is the momentum transfer to the scattered electron, and $\vec{p}_\pi$ is the detected pion momentum.

Following the conventions of the MAID group [15], the beam and target asymmetries can be expressed as

$$A_{LL} = -\sigma_{ez}/\sigma_0, \qquad (2)$$

$$A_{UL} = \sigma_z/\sigma_0, \qquad (3)$$

where

$$\sigma_{ez} = \sqrt{2\epsilon(1-\epsilon)}[P_x \sigma_{TL'x} \cos(\phi^*) + P_y \sigma_{TL'y} \sin(\phi^*)$$
$$+ P_z \sigma_{TL'z} \cos(\phi^*)] + \sqrt{1 - \epsilon^2}(P_x \sigma_{TT'x} + P_z \sigma_{TT'z}),$$

$$\sigma_z = \sqrt{2\epsilon(1+\epsilon)}(P_x \sigma_{TLx} \sin(\phi^*) + P_y \sigma_{TLy} \cos(\phi^*)$$
$$+ P_z \sigma_{TLz} \sin(\phi^*)) + \epsilon(P_x \sigma_{TTx} \sin(2\phi^*)$$
$$+ P_y \sigma_{TTy} \cos(2\phi^*) + P_z \sigma_{TTz} \sin(2\phi^*))$$
$$+ P_y(\sigma_{Ty} + \epsilon\sigma_{Ly}),$$

and

$$\sigma_0 = \sigma_T + \epsilon\sigma_L + \sqrt{2\epsilon(1+\epsilon)} \cos(\phi^*)\sigma_{TL}$$
$$+ \epsilon \cos(2\phi^*)\sigma_{TT},$$

where the direction cosines are defined as $P_z = \cos(\theta_q)$, $P_y = -\sin(\theta_q)\sin(\phi^*)$, and $P_x = \sin(\theta_q)\cos(\phi^*)$, and the virtual

TABLE II. Run period names, electron beam energy, and CLAS torus current of the different parts of the experiment analyzed. Also listed are the product of the absolute value of beam and target polarization for the polarized proton and deuteron runs (see Sec. IV F). The last two columns list the ratios of bound protons in the NH$_3$ and carbon targets ($R^p_{A>2}$) and bound neutrons in the ND$_3$ and carbon targets ($R^d_{A>2}$) (see Sec. IV H for full details).

Run period	Beam energy	I torus	$P_B P_T$(p)	$P_B P_T$(d)	$R^p_{A>2}$	$R^d_{A>2}$
Part 1p6i	1.603 GeV	1500 A	0.55	0.21	0.86	0.99
(Part 1p6o)	1.603 GeV	−1500 A	–	–	–	–
Part 1p7o	1.721 GeV	−1500 A	0.58	0.21	0.81	0.99
Part 2p2i	2.285 GeV	1500 A	0.50	–	0.86	–
Part 2p5i	2.559 GeV	1500 A	–	0.21	–	0.99
Part 2p5o	2.559 GeV	−1500 A	0.61	0.25	0.86	1.01
Part 4p2i	4.236 GeV	2250 A	0.54	0.18	0.85	0.99
Part 4p2o	4.236 GeV	−2250 A	0.55	0.18	0.88	1.01
Part 5p6i	5.612 GeV	2250 A	0.50	0.20	0.815	0.99
Part 5p72i	5.722 GeV	2250 A	0.50	0.20	0.815	0.99
Part 5p72o	5.722 GeV	−2250 A	0.50	0.19	0.83	0.99
(Part 5p74o)	5.740 GeV	−2250 A	0.50	0.19	–	–

TABLE III. Particles to be identified for each of the topologies of this analysis.

| Topology	Final state particles
$ep \to e\pi^+ n$	Electron, π^+, neutron
$ed \to e\pi^- p(p)$	Electron, π^-, proton
$ep \to e\pi^+(n)$	Electron, π^+
$ed \to e\pi^-(pp)$	Electron, π^-

photon polarization as

$$\epsilon = 1/[1 + 2(1 + \nu^2/Q^2)\tan^2(\theta_e)],$$

where ν is the virtual photon energy. The angles θ_e and θ_q are relative to the beam line direction for the scattered electron and the momentum transfer, respectively. The cross sections $\sigma_L, \sigma_T, \sigma_{TL}, \sigma_{TT}, \sigma_{TL'}$, and $\sigma_{TT'}$ are functions of the three variables W, Q^2, and θ^*.

In the case of π^- electroproduction from polarized deuterons, the above relations do not account for modifications from the proper treatment of the deuteron wave function (including the D state in particular) as well as final state interactions (such as charge-exchange reactions). These effects should be taken into account when interpreting the asymmetries presented in this paper in terms of reduced cross sections.

III. EXPERIMENT

The "eg1b" experiment used 1.6- to 5.7-GeV longitudinally polarized electrons from CEBAF at Jefferson Lab impinging on a 0.02 radiation length longitudinally polarized solid ammonia target immersed in liquid helium [16]. The target polarization direction is along the incident electron direction, *not* the direction of the momentum transfer vector, resulting
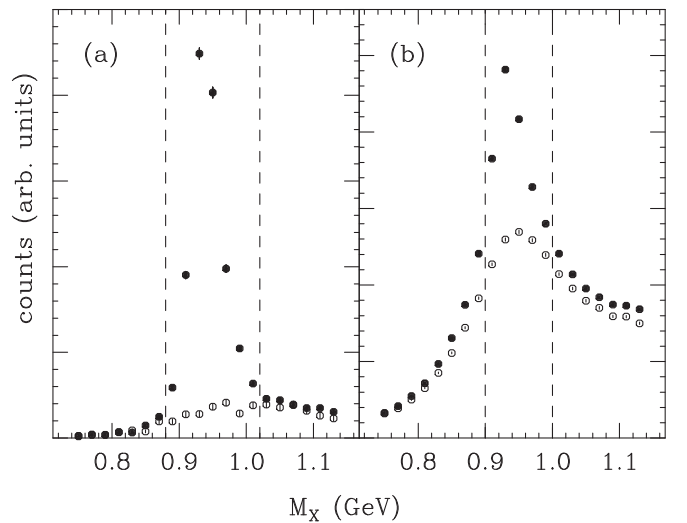
FIG. 1. Electron-pion missing mass spectra from Part 4p2o for the topology $ep \to e\pi^+ n$ (a) and topology $ep \to e\pi^+(n)$ (b). Counts from the ammonia NH$_3$ target are shown as the solid circles and counts from the carbon target (scaled by the ratio of integrated luminosities on bound nucleons) are shown as the open circles.
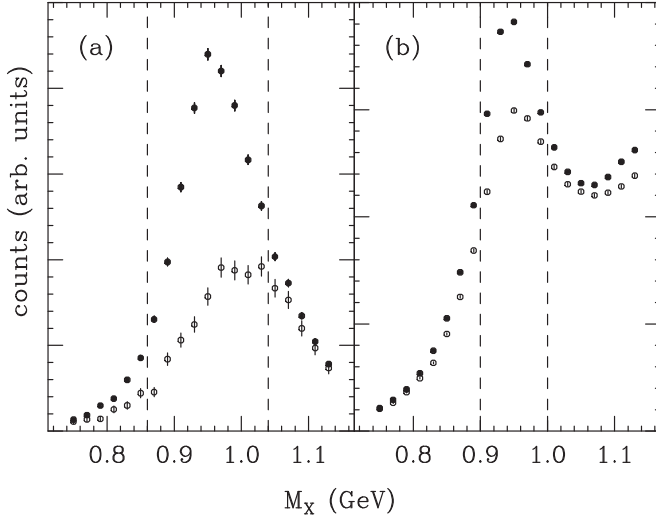
FIG. 2. Electron-pion missing mass spectra from Part 4p2o for the topology $ed \rightarrow e\pi^- p(p)$ (a) and topology $ed \rightarrow e\pi^-(pp)$ (b). Counts from the ammonia ND_3 target are shown as the solid circles and counts from the carbon target (scaled by the ratio of integrated luminosities on bound nucleons) are shown as the open circles.

in nonzero values of P_x and P_y. Scattered electrons and charged pions were detected in the CEBAF Large Acceptance Spectrometer (CLAS) [17]. The typical beam current was a few nA. The beam polarization, as periodically measured using Møller scattering in an upstream polarimeter, averaged 70%.

About 30% of the running time was on polarized protons ($^{15}NH_3$ target), 50% on polarized deuterons ($^{15}ND_3$ target), 13% on a reference unpolarized carbon target, and 2% on an empty cell (essentially a pure helium target). The ammonia targets used the ^{15}N isotope to simplify polarized nitrogen

FIG. 4. Distributions of angular differences in the predicted and observed nucleon direction cosines from Part 4p2o for topology $ep \rightarrow e\pi^+ n$ (left panels) and topology $ed \rightarrow e\pi^- p(p)$ (right panels). The top row is for $\delta\phi$ and the bottom row is for $\delta\theta$. The black points are for the ammonia target, while the open circles are from the carbon target, scaled by integrated luminosity. The vertical dashed lines indicate the cuts used in the analysis. All other relevant exclusivity cuts have been applied.

corrections. The 1.5-cm-diameter cups typically contained 0.7 g/cm^2 of material immersed in a 2-cm-long liquid-helium bath. The aerial densities of the target materials are listed in Table I. In this table, the thin Kapton foils that hold the ammonia beads have been merged with the aluminum beam
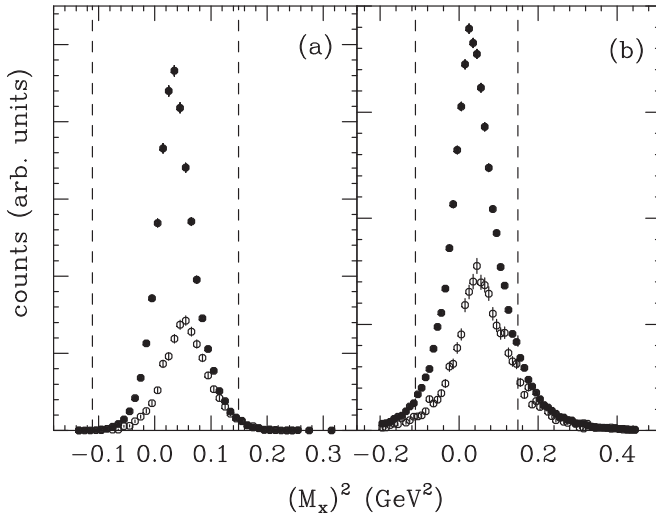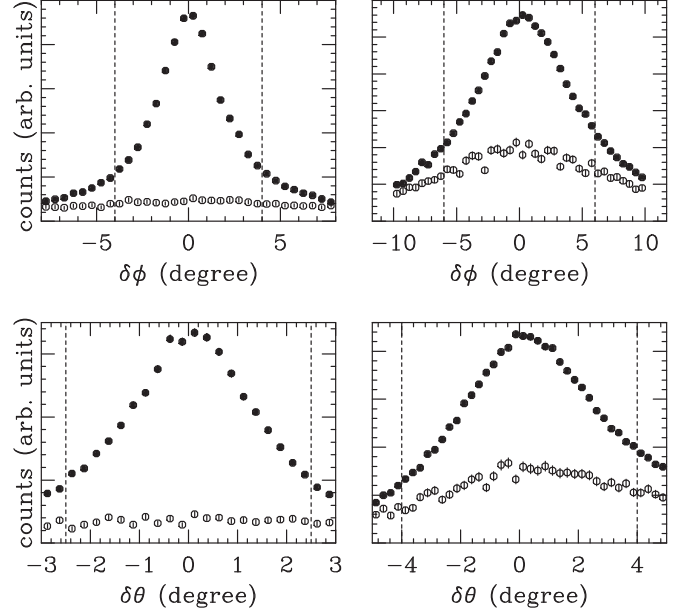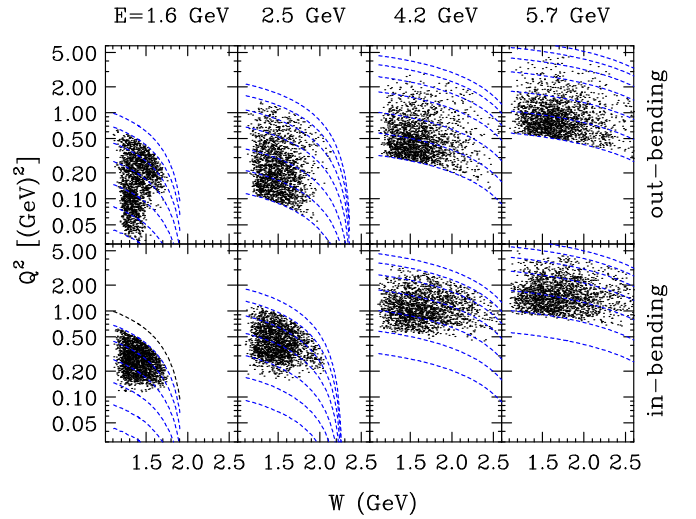

FIG. 3. Squared electron-proton missing mass spectra for the topology $ed \rightarrow e\pi^- p(p)$ for Part 1p6i (a) and Part 4p2o (b). Counts from the ND_3 target are shown as the solid circles and counts from the carbon target (scaled by the ratio of integrated luminosities on bound nucleons) are shown as the open circles. All other relevant exclusivity cuts have been applied.

FIG. 5. Distribution in (W, Q^2) of events for the $ep \rightarrow e\pi^+ n$ topology passing all exclusivity cuts, for four different beam energies, from left to right. The top (bottom) row of panels are for the out-bending (in-bending) torus polarity for negatively charged particles. The blue dashed lines show the bin limits in Q^2, defined by fixed bins in θ_e.

TABLE IV. Lower and upper limits of the cuts used on $M_x^{e\pi}$ for each of the relevant topologies.

Topology	Cut range
$ep \rightarrow e\pi^+ n$	$0.88 < M_x^{e\pi} < 1.02$ GeV
$ed \rightarrow e\pi^- p(p)$	$0.86 < M_x^{e\pi} < 1.04$ GeV
$ep \rightarrow e\pi^+ (n)$	$0.90 < M_x^{e\pi} < 1.00$ GeV
$ed \rightarrow e\pi^- (pp)$	$0.90 < M_x^{e\pi} < 1.00$ GeV

TABLE V. Cuts on $\delta\theta$ and $\delta\phi$ for each of the relevant topologies.

Topology	$\delta\theta$ cut	$\delta\phi$ cut
$ep \rightarrow e\pi^+ n$	$\|\delta\theta\| < 2.5°$	$\|\delta\phi\| < 4°$
$ed \rightarrow e\pi^- p(p)$	$\|\delta\theta\| < 4°$	$\|\delta\phi\| < 6°$

windows that contain the helium. The composition depends on two parameters, L and l_A.

To reduce the rate of depolarization of the target from radiation damage, the sub-millimeter-diameter beam was uniformly rastered over the 1.5-cm-diameter front face of the target every few seconds. The beam position, averaged over a few minutes or longer, was kept stable at the 0.1-mm level, using feedback from a set of beam position monitors. A split solenoid superconducting magnet provided a highly uniform 5-T magnetic field surrounding the target ($\delta B/B \approx 10^{-5}$).

Particles were detected in CLAS for polar angles from 8 to 48 degrees. CLAS comprises six azimuthally symmetric detector arrays embedded in a toroidal magnetic field. Charged particle momenta and scattering angles were measured with the drift chamber tracking system. The momentum resolution ranged from about 0.5% at 0.5 GeV to over 2% at 6 GeV. The resolution in polar angles was about 1 mrad, while the azimuthal angle resolution was typically 4 mrad. Electrons were separated from a significantly larger flux of charged pions using segmented gas Cherenkov detectors (CC, pion threshold
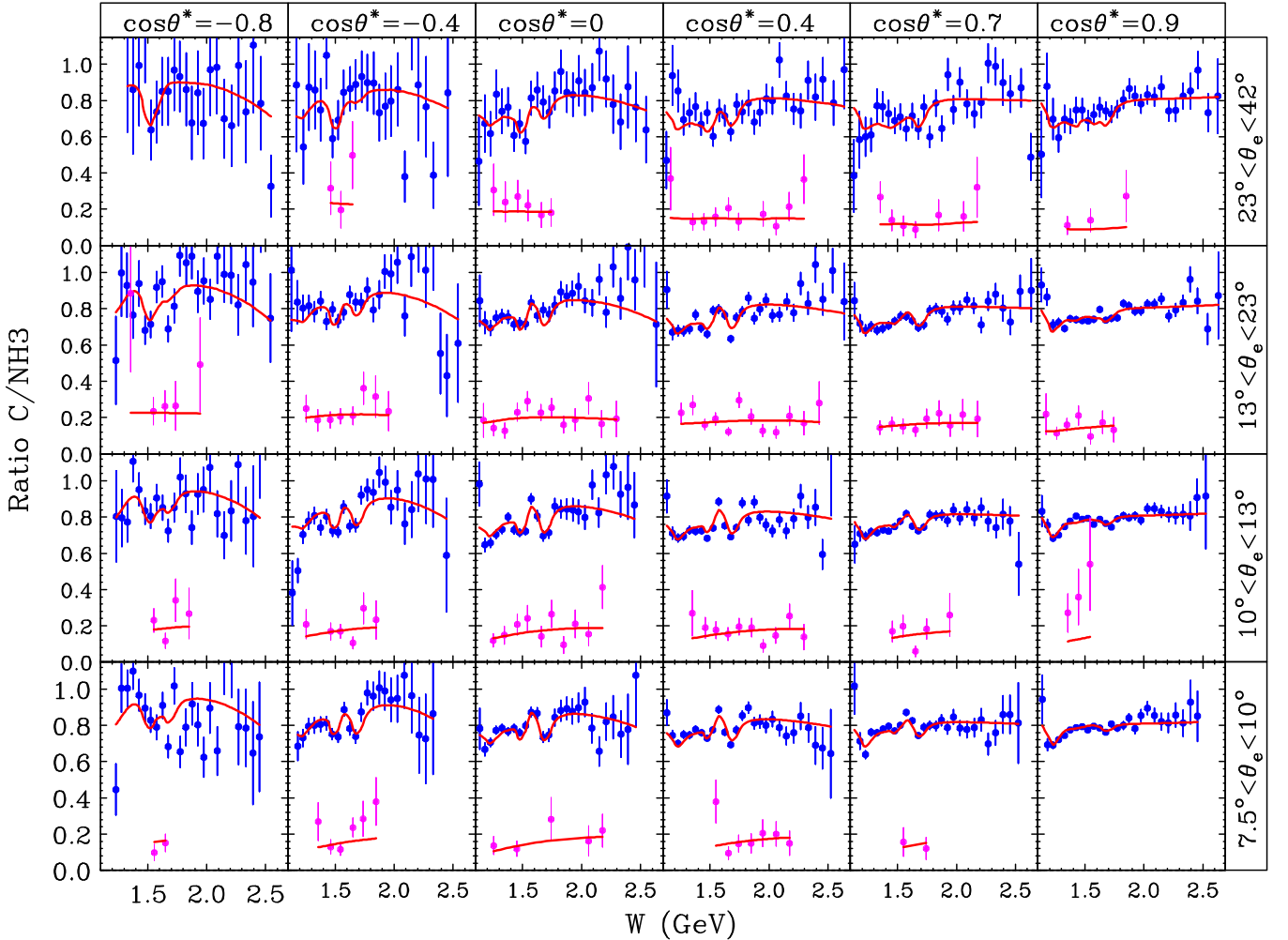

FIG. 6. Ratios of count rates from the carbon target to count rates from the NH$_3$ target for Part 4p2o of the experiment, for events passing all relevant exclusivity cuts. The panels correspond from left to right to six $\cos(\theta^*)$ bins and from bottom to top to four ranges of θ_e. The larger sets of ratios, shown in blue, correspond to the topology $ep \rightarrow e\pi^+(n)$, while the smaller values, shown in magenta, correspond to the fully exclusive topology $ep \rightarrow e\pi^+ n$. The red curves are the fits to the data described in the text (with the upper curves matching the blue points, and the lower curves matching the magenta points).
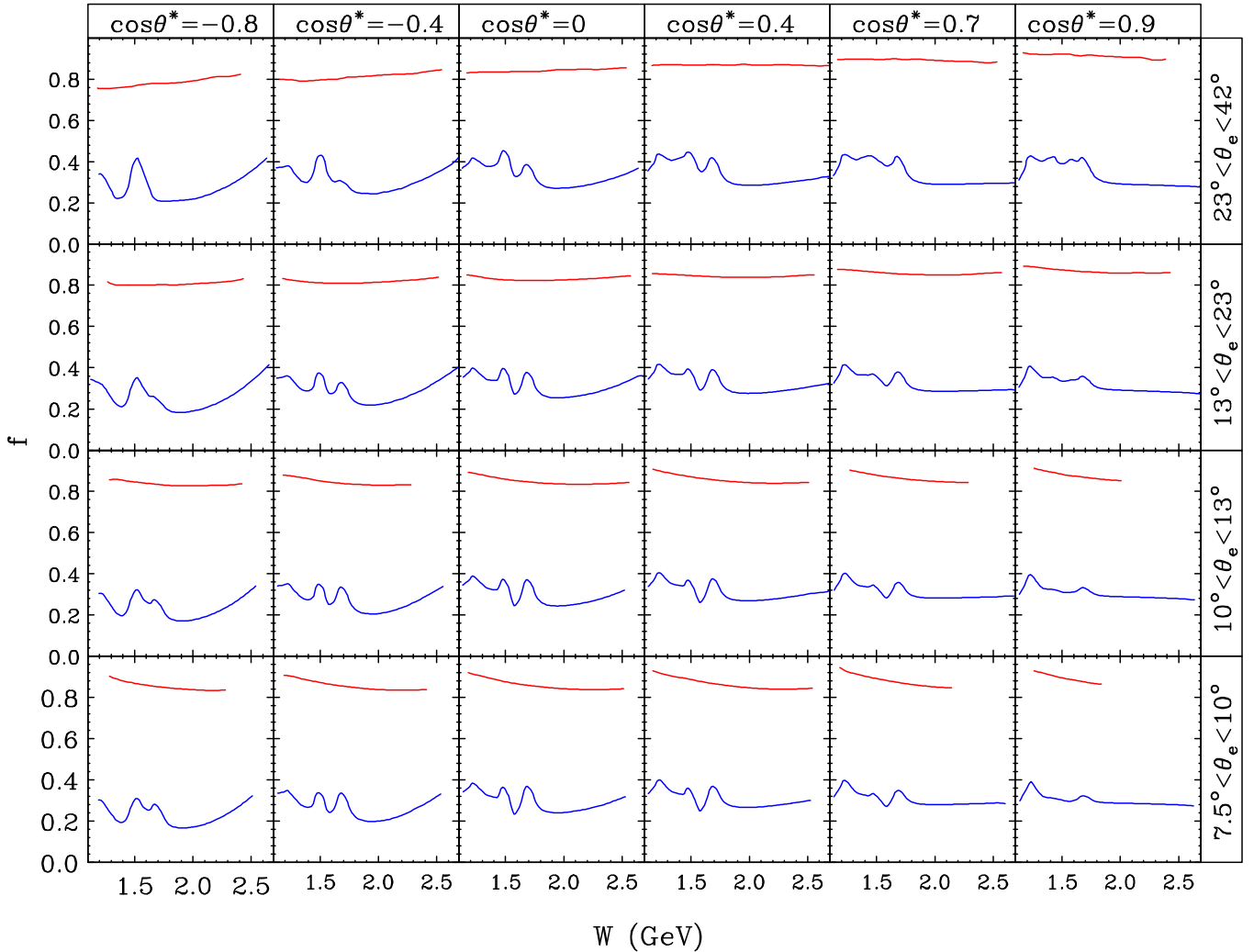
FIG. 7. Dilution factors as a function of W for the two π^+ topologies for Part 4p2o in six $\cos(\theta^*)$ bins (from left to right) and four θ_e bins (from bottom to top). The upper red curves within each panel correspond to topology $ep \to e\pi^+ n$ and the lower blue curves to topology $ep \to e\pi^+(n)$.

2.6 GeV) and a sampling electromagnetic calorimeter (EC). A layer of time-of-flight scintillator counters (SC) between the CC and EC was used for hadron identification. To not overwhelm the data acquisition system, the hardware trigger system was designed to have high efficiency for events with a scattered electron with an energy greater than 0.3 GeV, while rejecting other events. The hardware Cherenkov and calorimeter thresholds were adjusted to give a trigger rate of about 3000 Hz, with a dead time of about 10%. The distance from the target to the CLAS center was fixed at about -55 cm for the entire run.

The data taking took place in late 2000 and early 2001. The data set is divided into several parts, each with a different beam energy (2p5 for 2.5 GeV, etc.) and specific CLAS torus polarity ("i" or "o" for electron bending inward or outward in the torus). The field strength was three-quarters of standard full strength (corresponding to 3000 A) for those parts with beam energy above 4 GeV, and half of the standard value for the other parts. A summary is given in Table II. Both the $^{15}NH_3$ (proton) and

$^{15}ND_3$ (deuteron) targets were used for all parts except Part 2p5i, which only had the deuteron target, and Part 2p2i, which only had the proton target. Part 1p6o was not included in the final analysis, because data were taken only with the positive target polarization direction (for both NH_3 and ND_3), and both directions are needed to form target spin asymmetries. The relatively short Part 5p74o was not used because of corruption of the data taken with the carbon target (needed for luminosity normalization). Within each part used, some short running periods were removed because of problems with beam quality, target polarization, or detector performance.

One of the primary goals of the eg1b experiment was the measurement of spin structure functions through inclusive electron scattering, with results reported in Refs. [18–22]. Many experimental details can be found in these publications. Results for the other primary goal, which is the determination of charged pion electroproduction spin asymmetries, are the subject of the present paper and two Ph.D theses [23,24]. Results have also been published for neutral pion
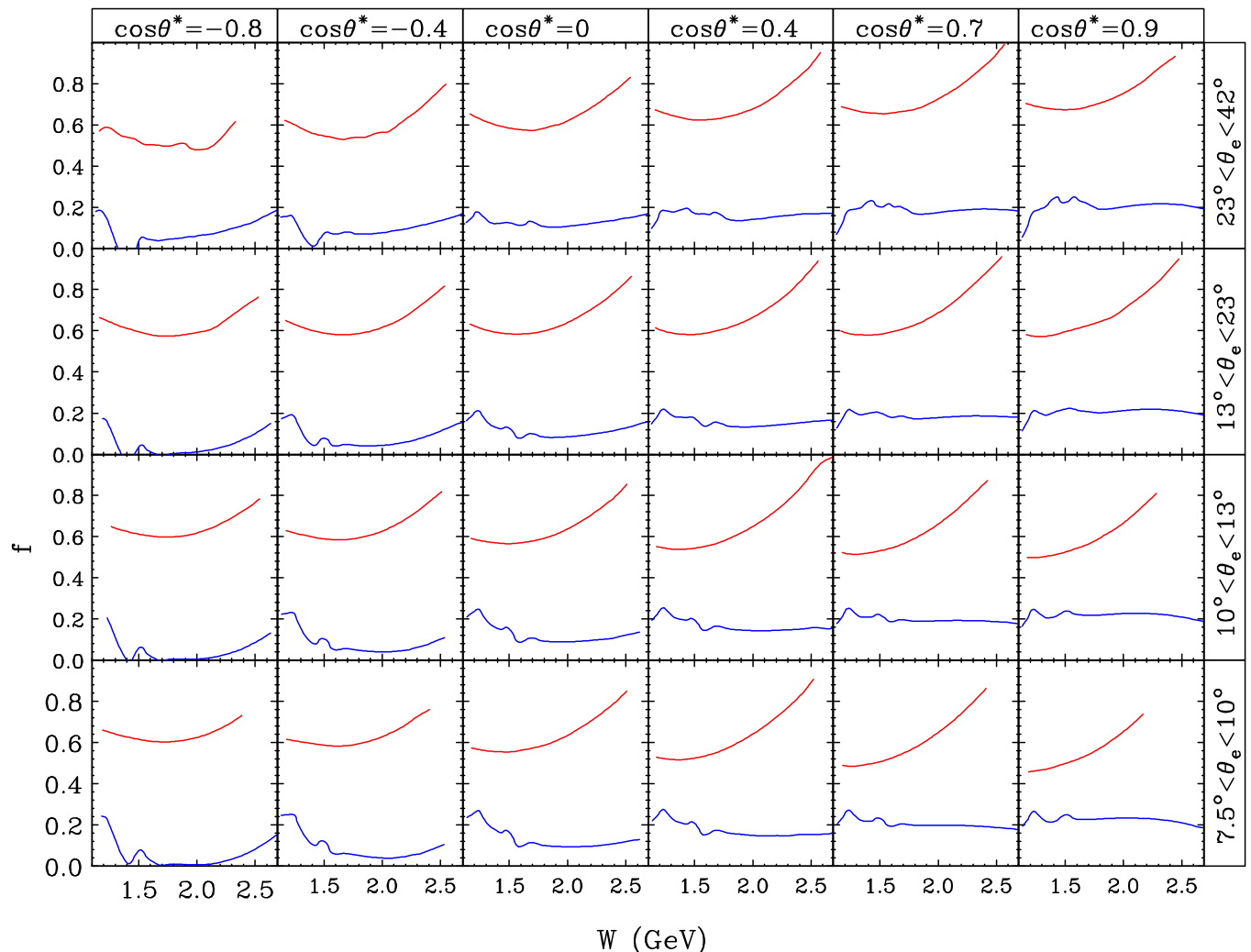
FIG. 8. Same as Fig. 7, except for the two π^- topologies: $ed \rightarrow e\pi^- p(p)$ (upper red curves) and $ed \rightarrow e\pi^-(pp)$ (lower blue curves).

electroproduction spin asymmetries for the lowest beam energy of the present experiment [25].

IV. ANALYSIS

A. Data processing

A subset of the data was used to calibrate the response of all of the CLAS detectors. The instruments that measured beam position and current were calibrated. The alignment of the detectors, as well as the target magnet, were also determined.

The raw data were passed through a standard CLAS analysis package that transformed raw timing and pulse-height signals into a set of "particles" for each trigger event. Direction cosines at the target were determined from the drift chambers for charged particles, and from the hit positions in the EC in the case of neutral particles. The momenta of charged particles were determined from the drift chamber tracks, while the energy of neutrals was determined from the EC. Charged-particle tracks were associated with the corresponding CC signals, EC energy deposition, and timing from the SC using geometrical

TABLE VI. Values of χ^2/d.f. and number of degrees of freedom (d.f.) for combining both asymmetries from the in-bending and out-bending torus polarity parts of each beam energy range.

| E_0 (GeV)	topology	A_{LL} χ^2/d.f.	d.f.	A_{UL} χ^2/d.f.	d.f.
1.7	$ed \rightarrow e\pi^- p(p)$	0.91	219	1.18	219
1.7	$ep \rightarrow e\pi^+(n)$	1.01	5001	1.13	4294
1.7	$ed \rightarrow e\pi^-(pp)$	1.03	1679	1.03	1679
2.5	$ep \rightarrow e\pi^+ n$	1.00	162	1.14	160
2.5	$ed \rightarrow e\pi^- p(p)$	1.00	588	1.08	588
2.5	$ep \rightarrow e\pi^+(n)$	1.04	7204	1.10	7197
2.5	$ed \rightarrow e\pi^-(pp)$	1.00	2893	1.07	2893
4.2	$ep \rightarrow e\pi^+ n$	1.00	310	1.12	310
4.2	$ed \rightarrow e\pi^- p(p)$	1.07	585	1.08	582
4.2	$ep \rightarrow e\pi^+(n)$	0.97	6799	1.10	6796
4.2	$ed \rightarrow e\pi^-(pp)$	0.98	2113	1.05	2107
5.7	$ep \rightarrow e\pi^+ n$	1.05	110	1.15	110
5.7	$ed \rightarrow e\pi^- p(p)$	0.97	207	0.99	207
5.7	$ep \rightarrow e\pi^+(n)$	0.99	4993	1.09	4993
5.7	$ed \rightarrow e\pi^-(pp)$	1.03	1314	1.09	1313
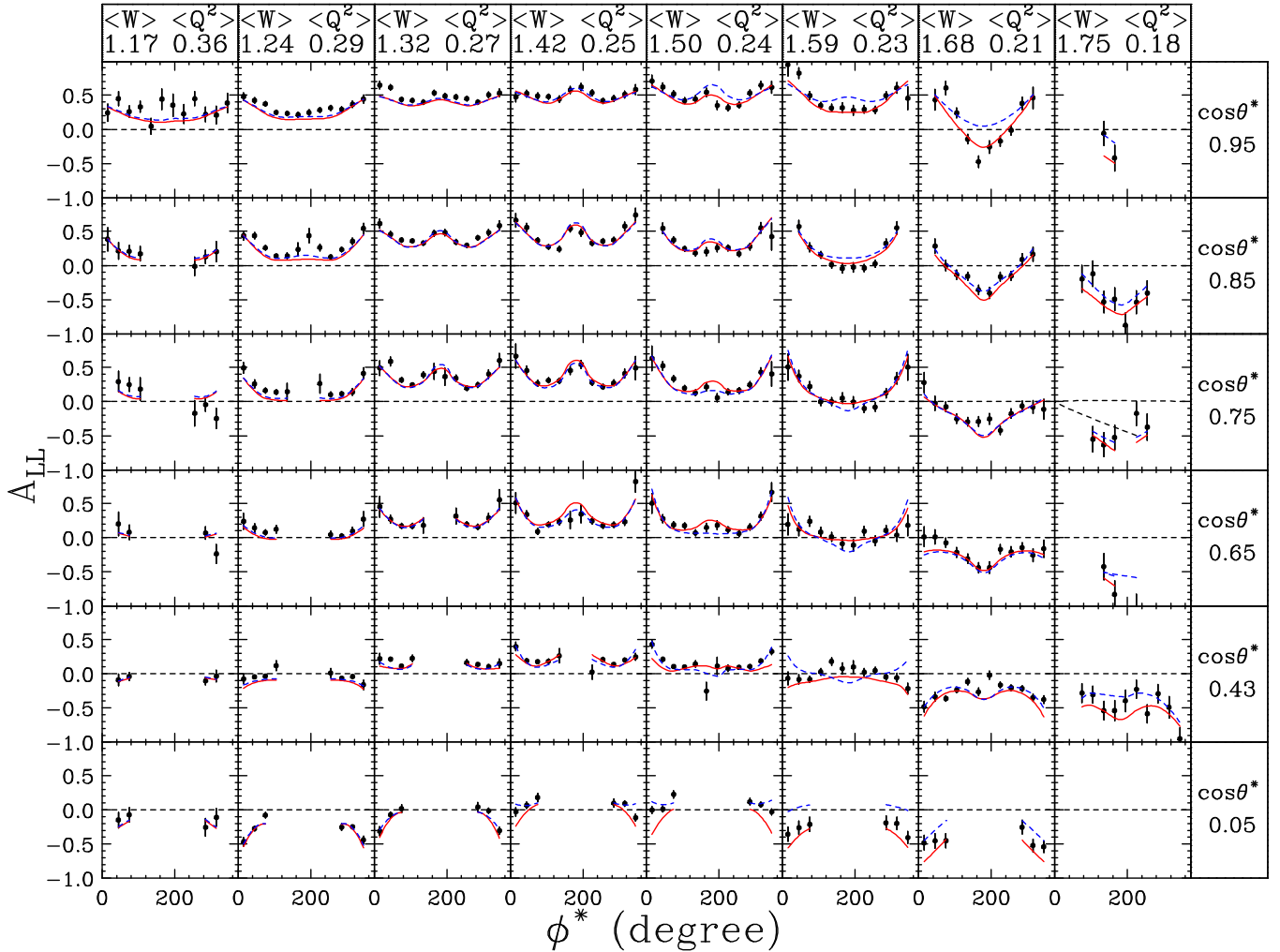
FIG. 9. Results for A_{LL} averaged over Q^2 as a function of ϕ^* in eight regions of W (left to right) and the six regions in $\cos(\theta^*)$ (top to bottom) for the reaction $ep \rightarrow e\pi^+n$ and a beam energy range of 1.6–1.7 GeV. The error bars do not include systematic uncertainties. The solid red curves are from MAID 2007 [15] and the dashed blue curves are from JANR [31]. The average values of W and Q^2 are in units of GeV and GeV^2, respectively. Only results with uncertainties less than 0.2 are plotted, along with the corresponding model curves. This results in some empty panels.

matching. Additional details can be found in the two archival papers describing the eg1b inclusive analysis [21,22].

A subset of the recorded events were subsequently written to skimmed data files for further processing. These data files only contained events that had a reasonable chance of passing the event selection cuts of the present analysis.

B. Particle identification

In the present analysis, we are interested in two reactions, $ep \rightarrow e\pi^+n$ and $ed \rightarrow e\pi^-p(p)$. For each reaction, we analyzed two distinct topologies, which were later combined. The four topologies are listed in Table III, along with the particles that must be identified in each case. The analysis of π^- electroproduction made the assumption that the interaction took place on a neutron and that the spectator proton was "invisible": Therefore both $ep \rightarrow e\pi^+n$ and $ed \rightarrow e\pi^-p(p)$ are referred to as "fully exclusive" topologies, and $ep \rightarrow e\pi^+(n)$ and $ed \rightarrow e\pi^-(pp)$ are referred to as

"one-missing-particle" topologies in the remainder of this article.

The fully exclusive and one-missing-particle topologies are distinct: In making the skim files, an event was put in the fully exclusive topology if a detected nucleon passed loose exclusivity cuts, else it was stored in the nonexclusive topology. If a fully exclusive event did not pass the slightly stricter cuts at the second level of processing, it was not moved over to the nonexclusive topology. Rather, the event was discarded completely, because such events predominantly originate from the nitrogen in the target.

1. Electron identification

Electrons were identified by requiring a signal of at least 2.5 photoelectrons in the CC, at least 67% of the electron energy to be deposited in the EC (front and back layers combined), and at least 6% of the electron energy to be deposited in the front layer of the EC. These cuts were needed to separate electrons

TABLE VII. Values of χ^2/d.f. and number of degrees of freedom (d.f.) for combining the two asymmetries from the topologies with all particles detected with the topology with a missing nucleon.

E_0 (GeV)	reaction	A_{LL} χ^2/d.f.	d.f.	A_{UL} χ^2/d.f.	d.f.
1.7	$ep \to e\pi^+ n$	1.01	433	1.13	428
1.7	$ed \to e\pi^- p(p)$	0.94	707	1.26	707
2.5	$ep \to e\pi^+ n$	1.00	1022	1.16	1000
2.5	$ed \to e\pi^- p(p)$	1.00	1555	1.20	1553
4.2	$ep \to e\pi^+ n$	1.05	1339	1.13	1336
4.2	$ed \to e\pi^- p(p)$	1.04	1588	1.06	1576
5.7	$ep \to e\pi^+ n$	1.02	663	1.18	662
5.7	$ed \to e\pi^- p(p)$	0.89	628	1.11	628

from pions, which would otherwise overwhelm the electron sample at the higher beam energies of this experiment. The track vertex position was required to be reconstructed within 3 cm of the nominal target center to remove backgrounds from the target chamber windows and heat shield foils. An additional cut to reduce pion contamination required that the track position in the SC be matched to the position in the CC.

2. Charged pion and proton identification

Charged hadrons were identified by requiring that the time of arrival at the scintillator counters be within 0.8 ns of that predicted from the time of arrival of the electron in the event. It was further required that charged pions and protons do not produce a significant signal in the CC (i.e., less than one photoelectron). A vertex cut of ± 3 cm was also required. Finally, particles produced at polar angles greater than 48 degrees in the laboratory frame were rejected because they passed through thick materials, causing significant energy loss and multiple scattering.

3. Neutron identification

Neutrons were identified by requiring the absence of a drift chamber track and a time of arrival at the EC corresponding to $\beta < 0.95$ to separate neutrons from photons. A further cut required an energy deposit of at least 0.3 GeV in the EC, to separate neutrons from low energy photons originating from an out-of-time interaction. The direction cosines of the neutron were determined from the EC hit coordinates. As discussed later, neutrons were only used to obtain a better dilution factor in exclusive π^+ production, so the cases where the neutron was
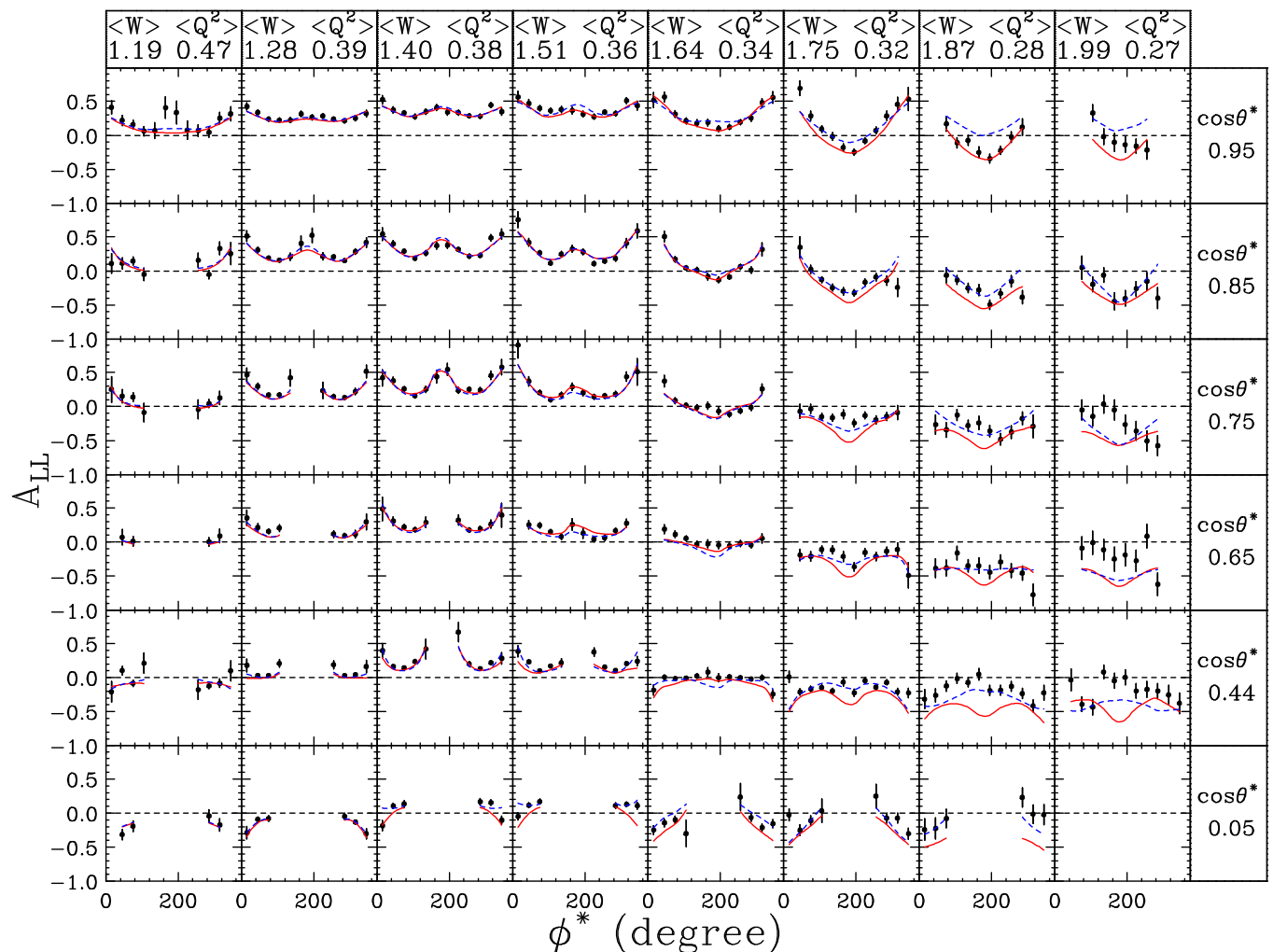

FIG. 10. Same as Fig. 9, except for a beam energy range of 2.2–2.5 GeV.

TABLE VIII. Estimated relative scale uncertainties for the various beam energies and asymmetries of the experiment from beam-target polarization, from dilution factor f, and from polarized nitrogen.

	$ep \rightarrow e\pi^+ n$							
	1.6 GeV		2.5 GeV		4.2 GeV		5.7 GeV	
Quantity	A_{LL}	A_{UL}	A_{LL}	A_{UL}	A_{LL}	A_{UL}	A_{LL}	A_{UL}
P_B, P_T	0.02	0.04	0.02	0.05	0.03	0.05	0.03	0.05
f	0.03	0.03	0.04	0.04	0.05	0.05	0.06	0.06
^{15}N	0.01	0.01	0.01	0.01	0.01	0.01	0.01	0.01
Total	0.04	0.05	0.05	0.07	0.06	0.07	0.07	0.08
	$ed \rightarrow e\pi^- p(p)$							
	1.6 GeV		2.5 GeV		4.2 GeV		5.7 GeV	
Quantity	A_{LL}	A_{UL}	A_{LL}	A_{UL}	A_{LL}	A_{UL}	A_{LL}	A_{UL}
P_B, P_T	0.05	0.06	0.07	0.07	0.10	0.10	0.15	0.15
f	0.10	0.10	0.12	0.12	0.15	0.15	0.20	0.20
^{15}N	0.02	0.02	0.02	0.02	0.02	0.02	0.02	0.02
Total	0.11	0.12	0.14	0.14	0.18	0.18	0.25	0.25

not identified simply moved events from $ep \rightarrow e\pi^+ n$ to $ep \rightarrow e\pi^+(n)$. The neutron momentum could not be determined from time of flight with sufficient accuracy to be useful.

C. Exclusivity kinematic cuts

For each of the four topologies, kinematic cuts were placed to improve the signal-to-noise ratio. The value of kinematic cuts is twofold. First, most of the kinematic quantities have a wider distribution for bound nucleons (in target materials with atomic number $A > 2$) than for free protons (or almost free neutrons in the deuteron). Kinematic cuts therefore reduce the dilution of the signal of interest (scattering from polarized free protons or quasifree neutrons), compared to the background from unpolarized nucleons in materials with $A > 2$. Furthermore, kinematic cuts are needed to isolate single meson production from multimeson production.

Many different kinematic cuts were found to be useful. All topologies used a cut on electron-pion missing mass. The topologies $ep \rightarrow e\pi^+ n$ and $ed \rightarrow e\pi^- p(p)$ had additional
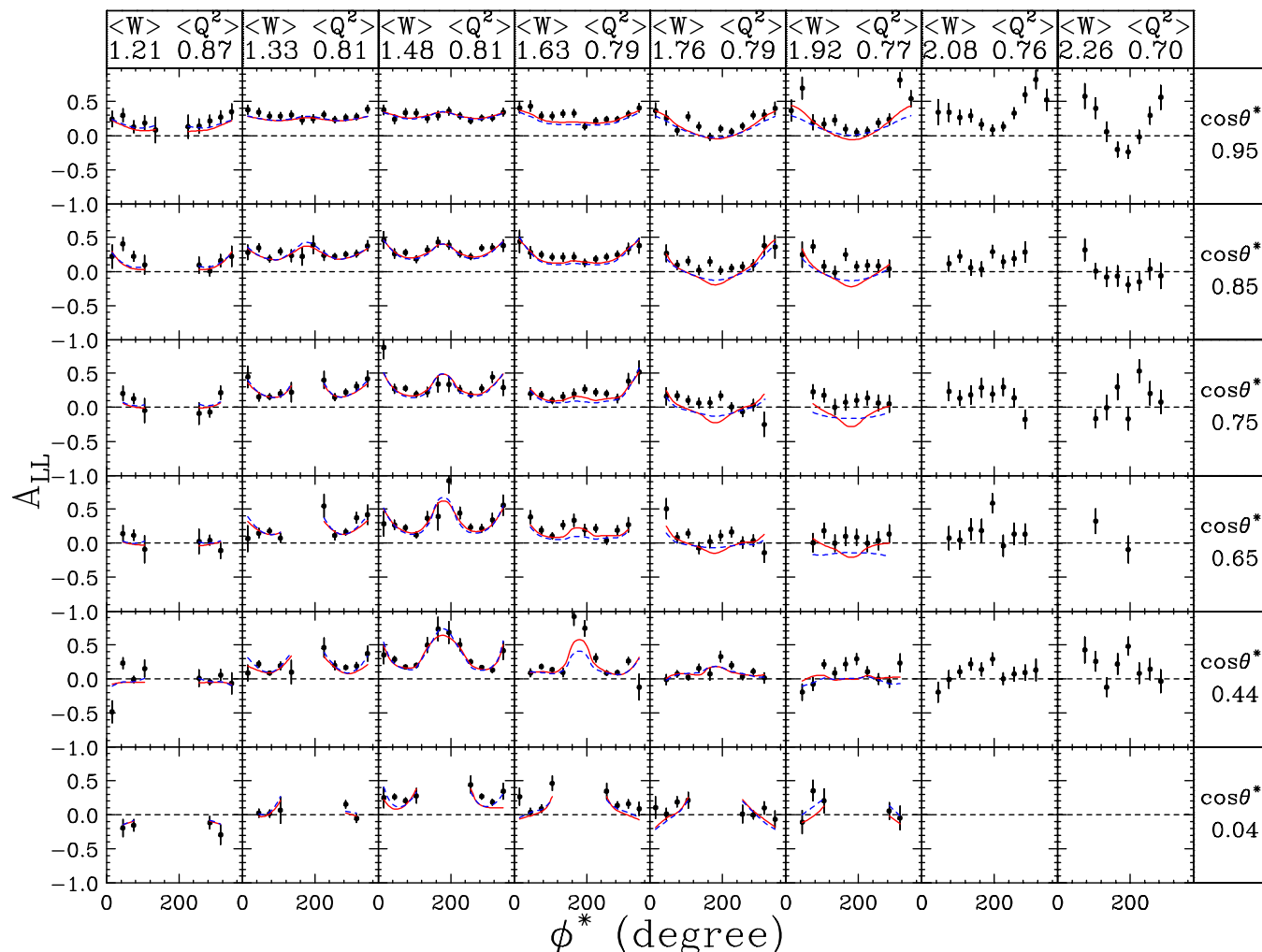

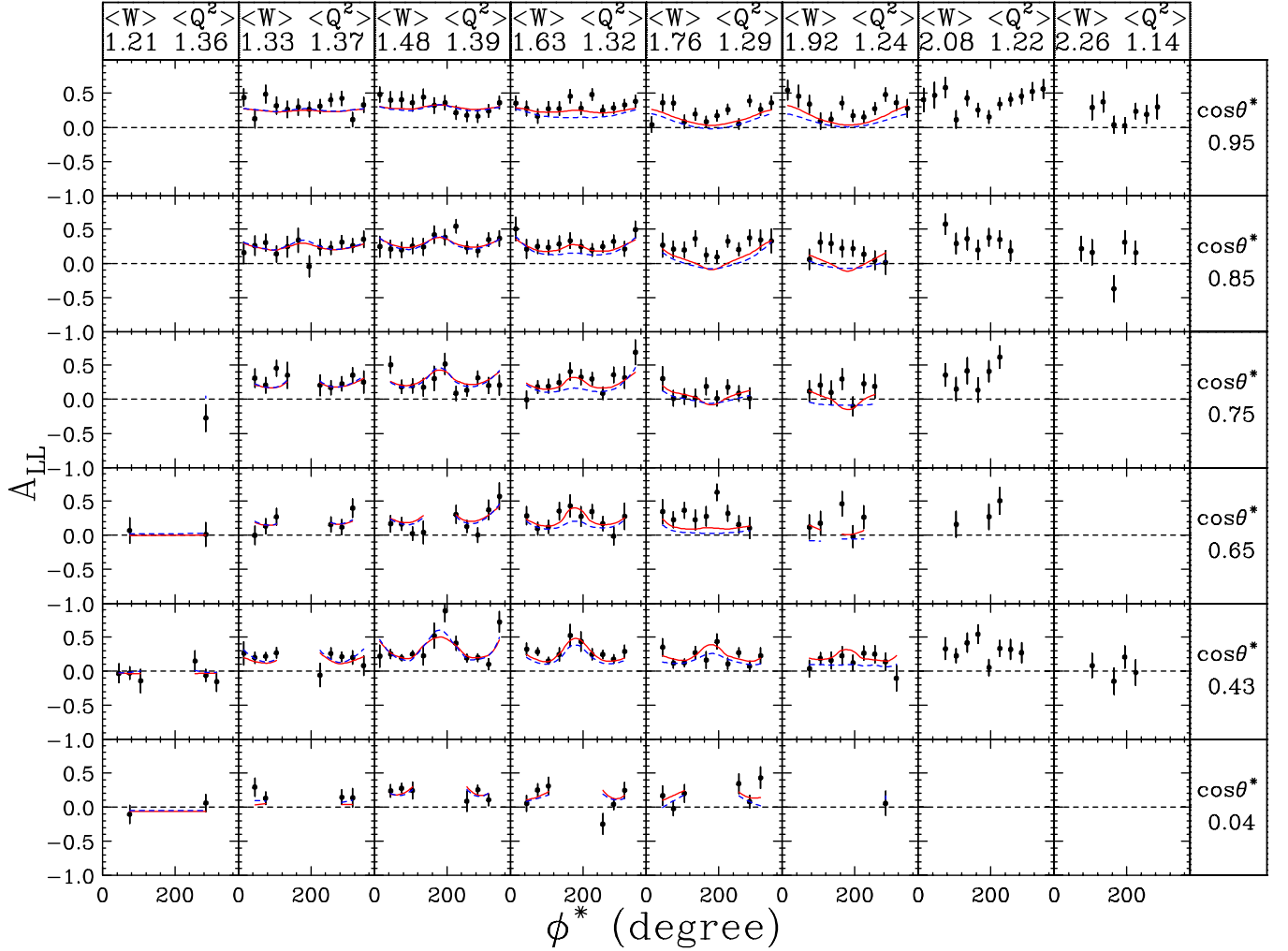FIG. 11. Same as Fig. 9, except for a beam energy of 4.2 GeV.

FIG. 12. Same as Fig. 9, except for a beam energy of 5.7 GeV.

cuts on the angles of the recoil nucleon. Topology $ed \rightarrow e\pi^- p(p)$ had additional cuts on the electron-proton missing mass and the electron-pion-proton missing energy. Details on all of these cuts are given in the sections below.

1. Electron-pion missing mass cuts

In all of the topologies studied, the electron-pion missing mass $M_x^{e\pi}$ should be equal to the nucleon mass M. In general, one would like the upper cut on $M_x^{e\pi}$ to be well below $M + m_\pi = 1.08$ GeV, to avoid contributions from multipion production, where m_π is the pion mass. Placing tighter cuts helps to reduce the nuclear background.

The spectra for $M_x^{e\pi}$ for topologies $ep \rightarrow e\pi^+ n$ and $ep \rightarrow e\pi^+(n)$ are shown in Fig. 1. For $ep \rightarrow e\pi^+(n)$, the missing mass was calculated assuming quasifree production from a neutron in the deuteron. The spectra are from Part 4p2o. The other cuts used for the $ep \rightarrow e\pi^+ n$ topology have been applied [no other cuts were used for $ep \rightarrow e\pi^+(n)$]. The solid circles correspond to counts from the ammonia target, while the open circles correspond to counts from the carbon target, scaled by the ratio of luminosities on $A > 2$ nucleons. A clear peak is

visible near the nucleon mass (0.94 GeV) from the ammonia target, with a smaller and much wider distribution from the carbon target. The wings of the ammonia distributions match well to the scaled carbon spectra on the low-mass side of the peaks, demonstrating that differences between nitrogen and carbon (and to a much smaller extent helium) because of final state interaction (FSI), Fermi motion, and other possible nuclear effects are relatively minor. On the high side of the peaks, the ammonia rates are higher, because of the radiative tail of the single-pion production. For the fully exclusive topology, the nuclear background is very small, while for the nonexclusive topology, the typical background is about half the signal size.

The spectra for $M_x^{e\pi}$ are shown for the two π^- topologies in Figs. 2(a) and 2(b). The peaks from the ND$_3$ target are wider than the corresponding peaks in the positive topologies because of the Fermi motion of neutrons in deuterium (which is about four times smaller than in $A > 2$ nuclei). This results in a larger nuclear background for the negative pion topologies than for the positive pion topologies.

The dashed vertical lines show the cuts used to minimize the final asymmetry uncertainties. The same cuts were used for all beam energies. The cut values are listed in Table IV.
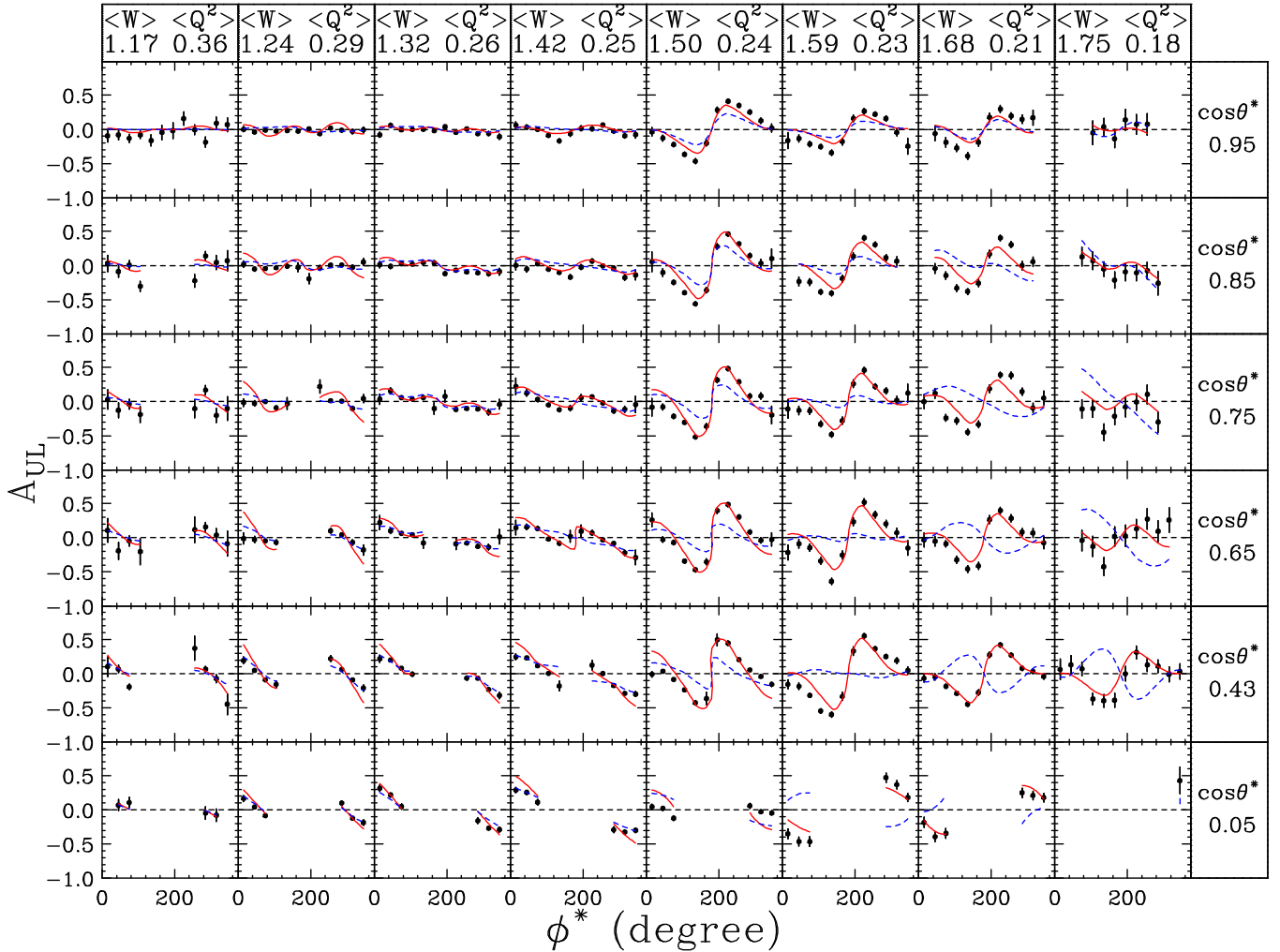
FIG. 13. Results for A_{UL} averaged over Q^2 as a function of ϕ^* in eight regions of W (left to right) and the six regions in $\cos(\theta^*)$ (top to bottom) for the reaction $ep \to e\pi^+ n$ and a beam energy range of 1.6–1.7 GeV. The error bars do not include systematic uncertainties. The solid red curves are from MAID 2007 and the dashed blue curves are from JANR [31]. Only results with uncertainties less than 0.2 are plotted, along with the corresponding model curves. This results in empty panels in some of the next figures.

2. Electron-proton missing mass cuts

In the case where there is a proton measured in the final state, the electron-proton missing mass M_x^{eN} should equal the pion mass, with the assumption of quasifree production. Distributions for the only relevant topology, $ed \to e\pi^- p(p)$ are shown in Fig. 3(a) for Part 1p6i and Fig. 3(b) for Part 4p2o. The background carbon distributions are somewhat similar to those from the ND$_3$ target, aside from a slight shift because of the higher average binding energy in $A > 2$ nuclei, so that only a modest reduction in background can be achieved. We used a single set of cuts for all beam energies: $-0.11 < (M_x^{eN})^2 < 0.15$ GeV^2.

3. Missing energy cut

In the topology $ed \to e\pi^- p(p)$, the energy of all the final state particles is measured, and therefore the missing energy E_m distribution should be centered around 2 MeV, assuming quasifree production from a deuteron. If the event came from a nucleus with $A > 2$, such as helium, nitrogen, or aluminum,

the missing energy will be larger, of order 20 MeV, because of the typical binding energy of a nucleon in a nucleus. Unfortunately the energy resolution of CLAS is not sufficient to clearly distinguish between quasifree and bound nucleons, but nevertheless we did find that placing an upper cut made a small improvement in the signal-to-background ratio. The cut $E_m < 0.065$ GeV was used for all kinematic bins and all parts.

4. Angular cuts

In the two topologies where all final state particles are detected, angular cuts are very useful in rejecting background from $A > 2$ materials. From the kinematics of the detected electron and meson, the direction cosines of the recoil nucleon are calculated, and compared with the observed angles. We denote the difference in predicted and observed angles as $\delta\theta$ in the in-plane direction and $\delta\phi$ in the out-of-plane direction (which tends to have worse experimental resolution). Distributions of these two quantities are shown for the relevant topologies in Fig. 4, averaged over all kinematic variables, for
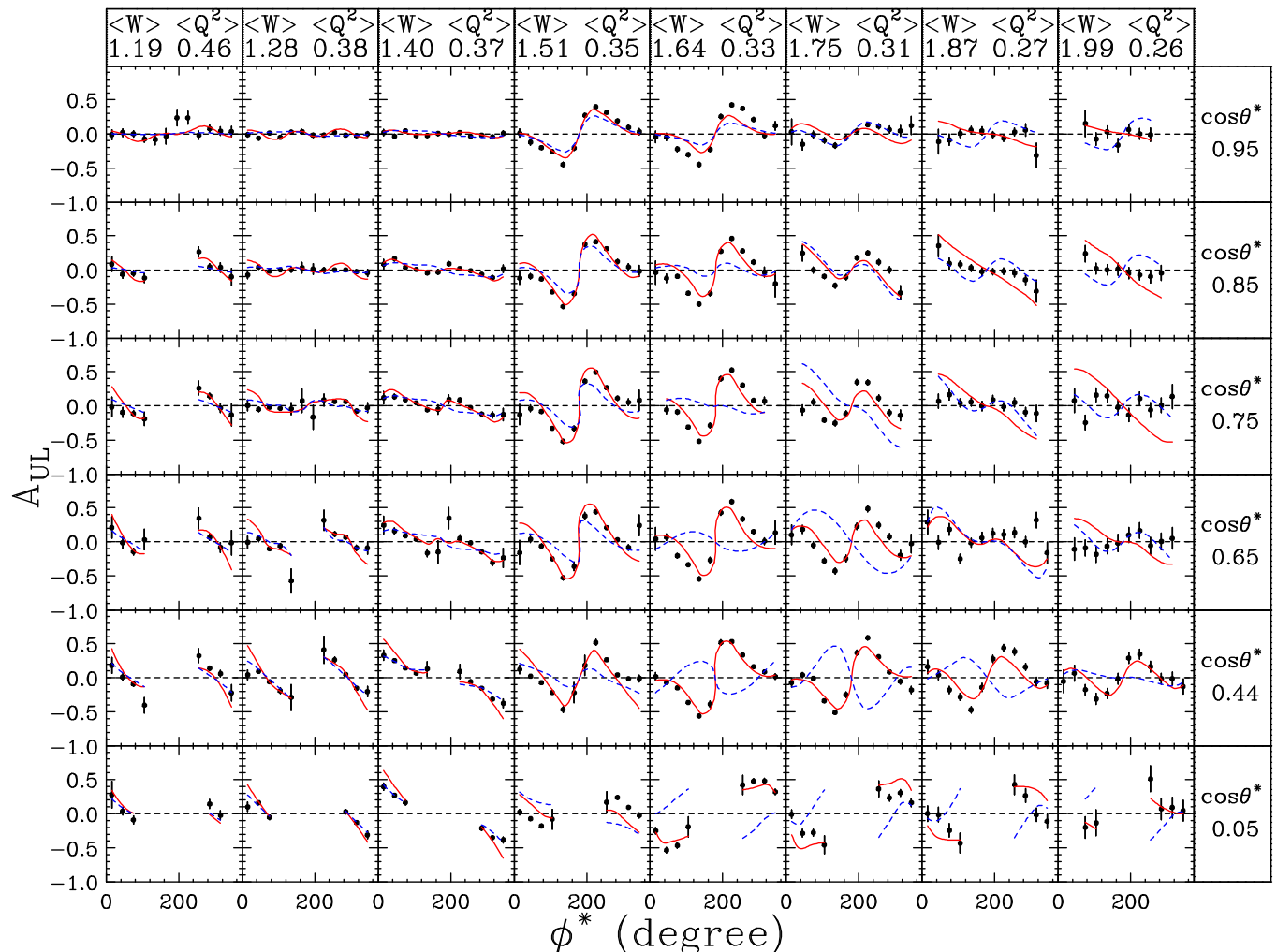
FIG. 14. Same as Fig. 13, except for a beam energy range of 2.2–2.5 GeV.

Part 4p2o. The dashed lines show the cuts used to optimize the signal-to-background ratio. The kinematic dependence of the angular resolution was found to be sufficiently weak to justify the use of a single cut value for all kinematic values. The cut values are listed in Table V.

D. Kinematic binning

The kinematic range of the experiment is $1.1 < W < 2.6$ GeV and $0.05 < Q^2 < 5$ GeV^2. As shown in Fig. 5, the range in Q^2 changes with W. We therefore made six bins in Q^2, where the limits correspond to electron scattering angles of 7.5, 10.0, 13.3, 17.6, 23.4, 31.0, and 42.0 degrees. To study possible resonance structure in the $ep \rightarrow e\pi^+ n$ reaction, we used nominal W bins of width 0.03, 0.04, or 0.05 GeV for beam energies near 1.7, 2.5, and 4.2–5.7 GeV, respectively. The bin widths increase slightly for $W > 2$ GeV. These bin sizes are comparable to the experimental resolution. For the $ed \rightarrow e\pi^- p(p)$ reaction, we used W bin widths that are three times larger than for the $ep \rightarrow e\pi^+ n$ reaction (i.e., 0.09, 0.12, or 0.15 GeV). This sacrifice was made so the majority of bins

had at least 10 counts (the minimum needed for Gaussian statistical uncertainties).

An examination of event rates showed a strong forward peaking in $\cos(\theta^*)$ for all the topologies studied, roughly independent of (W, Q^2). We use 12 bins in $\cos(\theta^*)$, with boundaries at -1.0, -0.8, -0.6, -0.4, -0.2, 0, 0.2, 0.4, 0.6, 0.7, 0.8, 0.9, and 0.995. Finer bins in $\cos(\theta^*)$ were used for $\cos(\theta^*) > 0$ because the cross sections tend to be forward peaked, especially at the higher values of W and Q^2. Because the pion polar angle was limited to 48 degrees in the laboratory frame, most of the bins with $\cos(\theta^*) < 0$ are empty. The uppermost boundary of 0.995 was chosen instead of 1.0 because the average resolution in ϕ^* becomes worse than 30 degrees above $\cos(\theta^*) = 0.995$, making it increasingly problematic to determine the ϕ^* dependence of spin asymmetries at very forward angles.

We use 12 bins in ϕ^*, equally spaced between 0 and 2π. We chose 12 bins to be able to distinguish between terms proportional to $\sin(\phi^*)$ and those proportional to $\sin(2\phi^*)$.

For most bins, the average values of $(W, Q^2, \cos(\theta^*), \phi^*, \epsilon)$ are very close to the bin centers. No bin-centering corrections were applied to the data. Instead, the count-weighted average
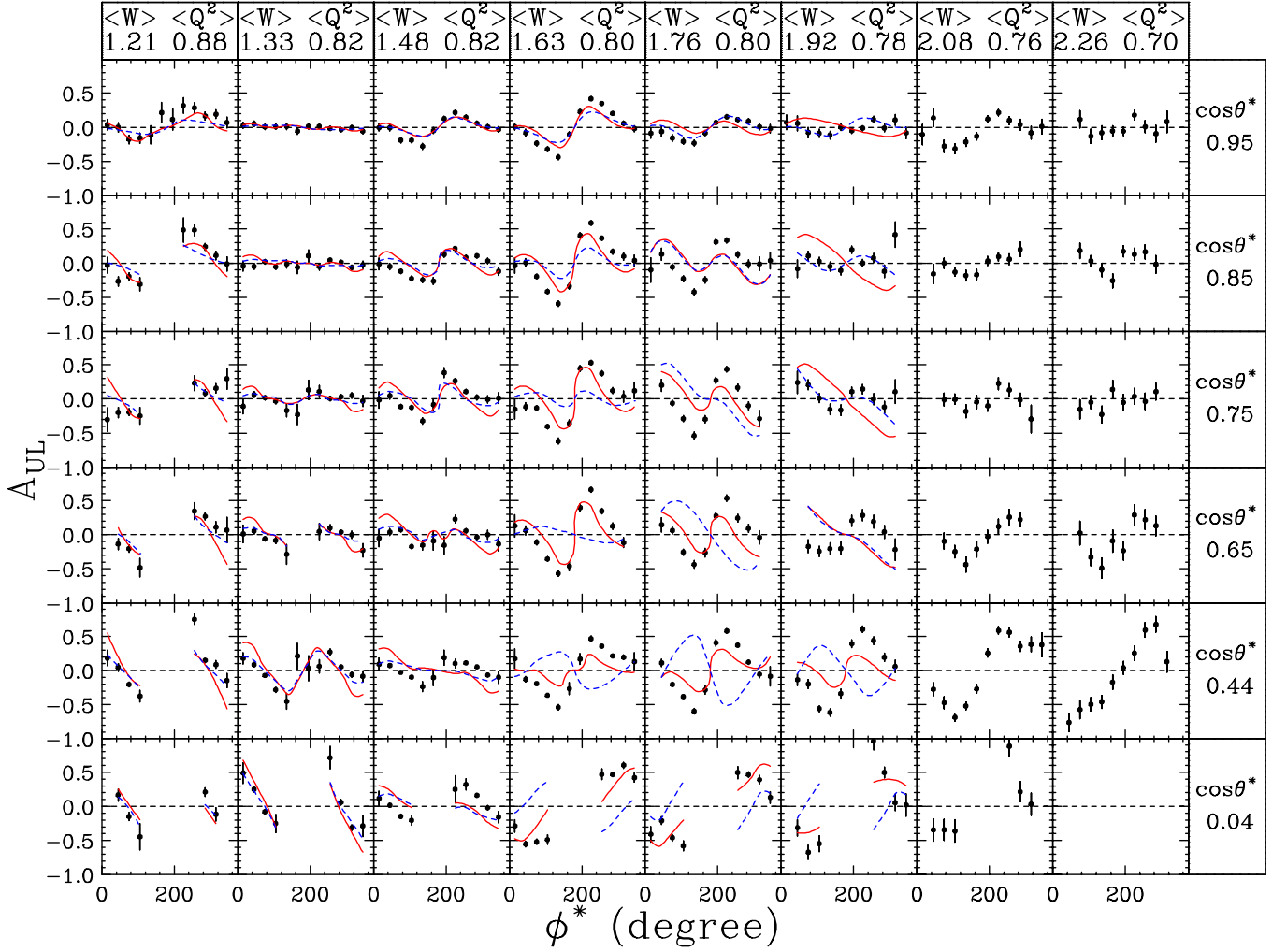
FIG. 15. Same as Fig. 13, except for a beam energy of 4.2 GeV.

values of all relevant kinematic variables are included in the table of results [26,27].

The values of $(W, Q^2, \cos(\theta^*), \phi^*, \epsilon)$ were obtained assuming that the struck nucleon is at rest, which is a valid assumption for the $ep \to e\pi^+ n$ reaction, but not the $ed \to e\pi^- p(p)$ reaction. In the latter case, the typical momentum of the struck nucleon is of order 0.05 GeV, which introduces an uncertainty in $(W, Q^2, \cos(\theta^*), \phi^*)$ that is less than, or in the worst case, comparable to the chosen bin sizes for this reaction.

E. Asymmetries

Spin asymmetries were formed as follows:

$$A_{LL} = \frac{N^{\uparrow\downarrow} + N^{\downarrow\uparrow} - N^{\uparrow\uparrow} - N^{\downarrow\downarrow}}{N_{\text{tot}} \ f \ P_B P_T}, \quad (4)$$

$$A_{UL} = \frac{N^{\uparrow\uparrow} + N^{\downarrow\uparrow} - r_T N^{\uparrow\downarrow} - r_T N^{\downarrow\downarrow}}{N_{\text{tot}} \ f \ P_T}, \quad (5)$$

where the symbols N represent the number of events in a given helicity configuration, divided by the corresponding integrated beam current. The first superscript refers to the beam polarization direction and the second to the target polarization

direction. Here $N_{\text{tot}} = N^{\uparrow\uparrow} + N^{\downarrow\uparrow} + N^{\uparrow\downarrow} r_T + N^{\downarrow\downarrow} r_T$, and f is the dilution factor, defined as the fraction of events originating from polarized nucleons compared to the total. The factor r_T is the ratio of effective target thicknesses for data taken with positive and negative target polarization (reversal frequency typically three days) and ranged from 0.98 to 1.02, except for the deuteron runs of Part 5p7i, where the correction was 0.94. No correction was needed for running with positive and negative beam helicity from the rapid (30 Hz) reversal rate. The target polarization P_T is the luminosity-weighted average of the absolute value of the positive and negative target polarization data. The effect of the small difference in absolute value of negative and positive target polarizations is taken into account through our method of determining $P_B P_T$ from ep elastic (quasielastic) scattering.

The sign convention for A_{LL} corresponds to a positive value when the cross section for scattering to a spin $S = \frac{1}{2}$ final state is larger than to a $S = \frac{3}{2}$ final state (see Sec. II).

F. Beam and target polarization

The product of beam polarization (P_B) and target polarization (P_T) was determined using the well-understood
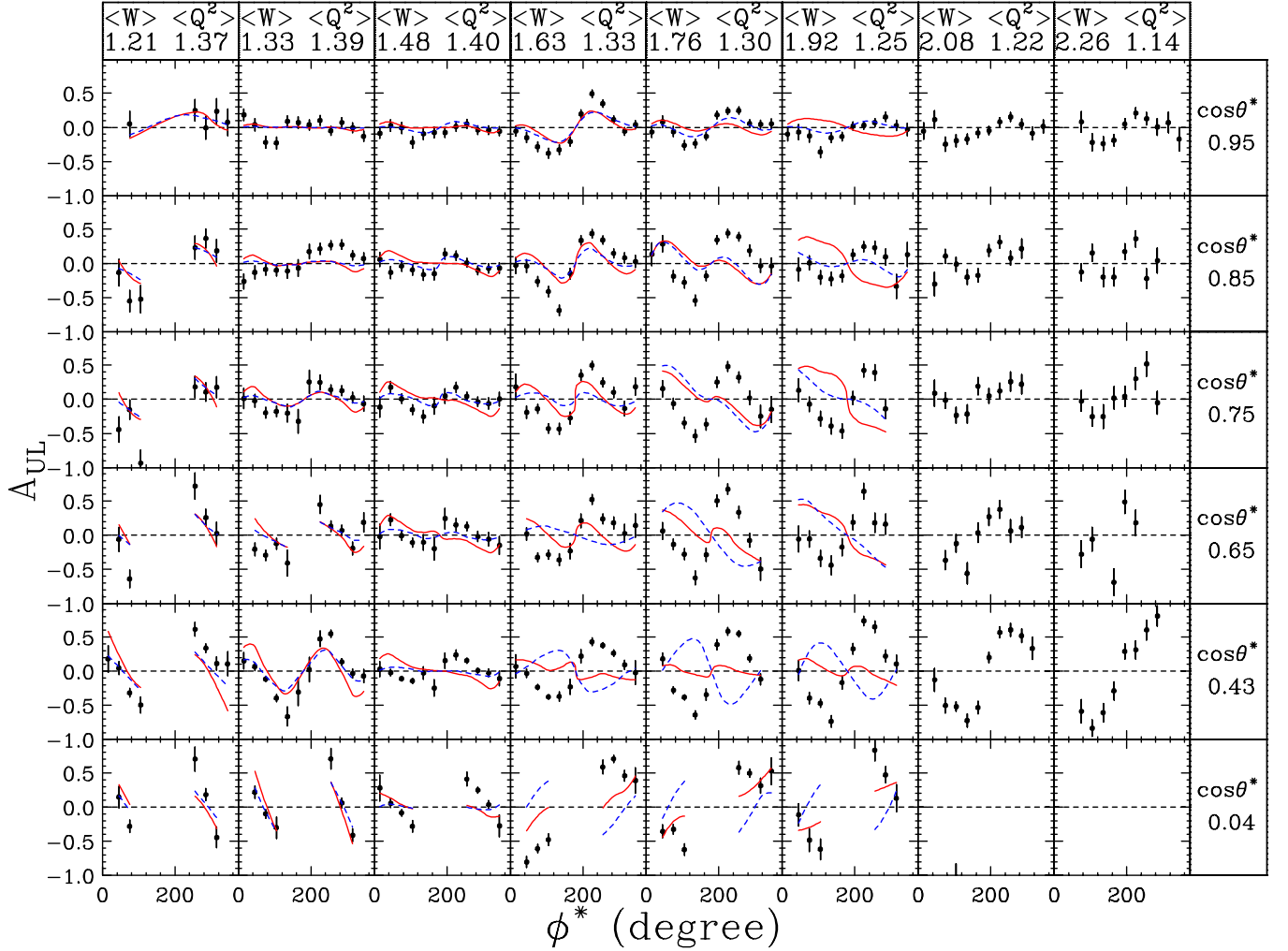
FIG. 16. Same as Fig. 13, except for a beam energy of 5.7 GeV.

beam-target spin asymmetry in elastic ep scattering (quasielastic scattering for the deuteron target). The results [21,22] are listed in Table II. The beam polarization was measured using Møller scattering. The average value was 0.70, with a spread of about 4% (relative). No dependence on incident beam energy was observed. For determining the target spin asymmetry A_{UL}, the proton or deuteron target polarization was determined by dividing the values of $P_B P_T$ from ep elastic scattering by P_B from the Møller measurements.

G. Combining similar parts

The number of events as well as the average value of kinematic quantities was stored for each kinematic bin for each part separately. Before extracting the dilution factor and asymmetries, the counts and averaged kinematic quantities were combined for Parts 5p6i and 5p72i and the result is named Part 5p7i.

H. Dilution factor

The dilution factor f is defined as the ratio of scattering rate from free nucleons to the scattering rate from all nucleons in the target. If we make the assumption that the cross section

per nucleon is the same for bound protons in all of the nuclear materials (with $A > 2$) [28] in a given target, and also that the effective detection efficiency is the same for the ammonia and carbon targets, then

$$f = 1 - R_{A>2} \frac{N_C}{N_{NX_3}}, \qquad (6)$$

where N_C and N_{NX_3} are the number of counts measured in a given kinematic bin for a given topology, normalized by the corresponding integrated beam charge, and $R_{A>2}$ is the ratio of the number of bound nucleons in the ammonia target to the number of bound nucleons in the carbon target. Bound nucleons are defined to be in materials with atomic number $A > 2$. The latter was determined from a detailed analysis of the target composition using inclusive electron scattering rates from ammonia, carbon, and empty targets [21,22]. The ratio must be determined separately for bound protons in the NH_3 target (for the $ep \rightarrow e\pi^+ n$ reaction) and for bound neutrons in the ND_3 target [for the $ed \rightarrow e\pi^- p(p)$ reaction]. We denote these ratios as $R_{A>2}^p$ and $R_{A>2}^d$, respectively, and list the values used in the analysis in Table II. Using a study of inclusive electron scattering rates, we found $R_{A>2}^p$ to vary between 0.81 and 0.86 for the various parts of the experiment, while
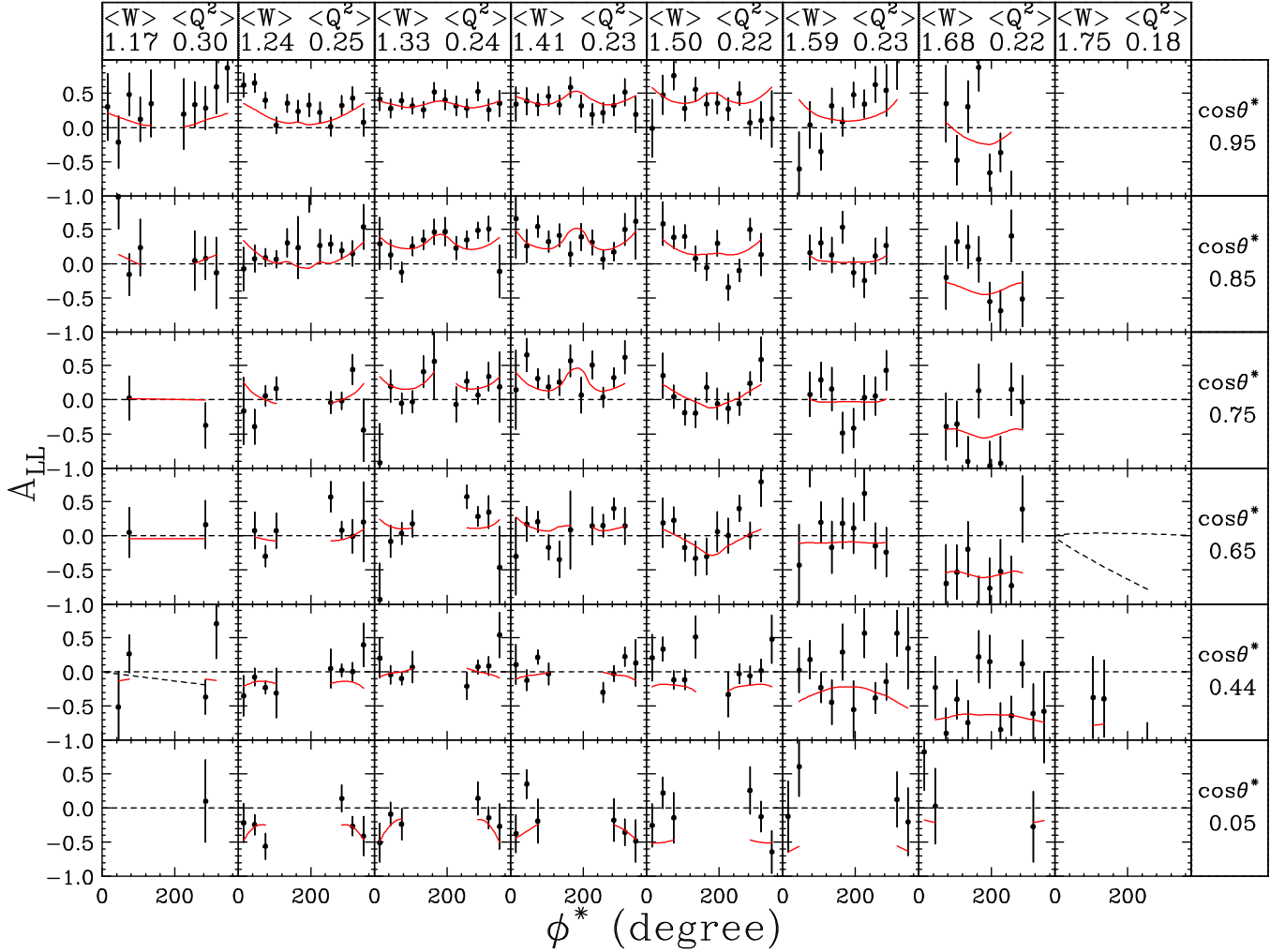
FIG. 17. Results for A_{LL} averaged over Q^2 as a function of ϕ^* in eight regions of W (left to right) and the six regions in $\cos(\theta^*)$ (top to bottom) for the reaction $ed \rightarrow e\pi^- p(p)$ and a beam energy range of 1.6–1.7 GeV. The error bars do not include systematic uncertainties. The curves are from MAID 2007. Only results with uncertainties less than 0.6 are plotted, along with the corresponding model curves. This results in some empty panels.

$R_{A>2}^d$ varied between 0.99 and 1.01. The variation is because of the target material being replaced periodically during the experiment, and also because of settling of the ammonia beads.

Because the integrated luminosities on the carbon target were generally about five times lower than on the ammonia targets, there is a large amplification of the uncertainty on the ratio of carbon to ammonia counts, $\frac{N_C}{N_{NX_3}}$. In many cases, this would lead to unphysical values of f (i.e., $f < 0$). We therefore took advantage of the fact that f is a very slowly varying function of kinematic variables, and did a global fit to $\frac{N_C}{N_{NX_3}}$ for each topology and run configuration. The fit values were then used to evaluate f in each kinematic bin.

Several functional forms for the fits to $\frac{N_C}{N_{NX_3}}$ were tried. The final form selected was

$$\frac{N_C}{N_{NX_3}} = P_1[1 + P_2 W + P_3 Q^2 + P_4 \cos(\theta^*)$$
$$+ P_5 W^2 + P_6 W Q^2 + P_7 W \cos(\theta^*) + P_8 (Q^2)^2$$

$$+ P_9 W Q^2 \cos(\theta^*) + P_{10} \cos(\theta^*)^2 + P_{11} R_1(W^2)$$
$$+ P_{12} R_2(W^2) + P_{13} R_3(W^2) + P_{14} W^2 \cos(\theta^*)$$
$$+ P_{15} R_1(W^2) \cos(\theta^*) + P_{16} R_2(W^2) \cos(\theta^*)$$
$$+ P_{17} R_3(W^2) \cos(\theta^*) + P_{18} R_2(W^2) \cos(\theta^*) Q^2$$
$$+ P_{19} R_3(W^2) \cos(\theta^*) Q^2 + P_{20} R_2(W^2) \cos(\theta^*)^2$$
$$+ P_{21} R_3(W^2) \cos(\theta^*)^2 + P_{22} R_2(W^2) Q^2$$
$$+ P_{23} R_3(W^2) Q^2 + R_4(W^2)(P_{24} + P_{25} \cos(\theta^*))$$
$$+ P_{26} Q^2 + P_{27} \cos(\theta^*) Q^2 + P_{28} \cos(\theta^*)^2)$$
$$+ R_5(W^2)(P_{29} + P_{30} \cos(\theta^*) + P_{31} Q^2$$
$$+ P_{32} \cos(\theta^*) Q^2 + P_{33} \cos(\theta^*)^2)],$$

where the functions,

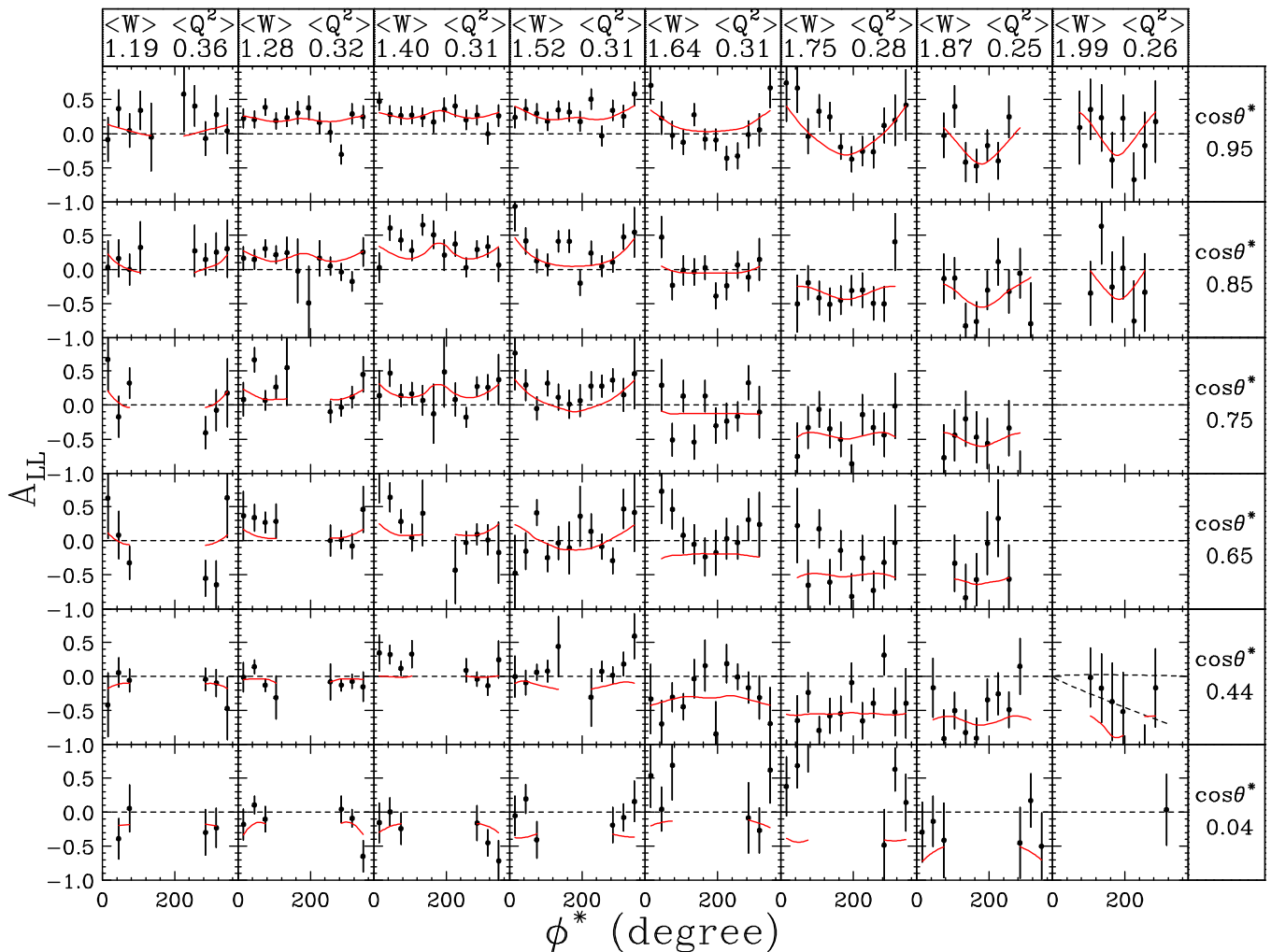$$R_i(W^2) = \frac{\Gamma_i}{(W^2 - W_i^2)^2 + (W_i \Gamma_i)^2}, \qquad (7)$$

FIG. 18. Same as Fig. 17, except for a beam energy range of 2.2–2.5 GeV.

are to account for the influence of the five prominent resonances [15] at $W_1 = 1.23$ GeV, $W_2 = 1.53$ GeV, $W_3 = 1.69$ GeV, $W_4 = 1.50$ GeV, $W_5 = 1.43$ GeV, and with widths $\Gamma_1 = 0.135$ GeV, $\Gamma_2 = 0.220$ GeV, $\Gamma_3 = 0.120$ GeV, $\Gamma_4 = 0.080$ GeV, and $\Gamma_5 = 0.370$ GeV. The reason that these resonance terms are needed is that the nucleon resonances are very much broadened in the target materials with $A > 2$, but have the natural width for free nucleons. This generates resonantlike structures in the ratio of carbon to ammonia count rates. The other terms are simply power-law expansions in terms of W, Q^2, and $\cos(\theta^*)$.

All of the fit parameters were used for the highest-statistical accuracy topologies $ep \rightarrow e\pi^+(n)$ and $ed \rightarrow e\pi^-(2p)$. For the low count rate topologies $ep \rightarrow e\pi^+n$ and $ed \rightarrow e\pi^-p(p)$, parameters 8–10 and 14–33 were fixed at zero. Tests were made to see if any ϕ^*-dependent terms would improve the fits. No significant improvements were found. Comparisons of fits and data are made for the two π^+ topologies in Fig. 6 for Part 4p2o. The data show considerable resonance structure, and this part was the most difficult to obtain a good fit.

The dilution factors were evaluated using Eq. (6) and the fits to $\frac{N_C}{N_{NX_3}}$. The results for the two π^+ topologies are

shown for Part 4p2o in Fig. 7 as a function of W in a grid over θ_e and $\cos(\theta^*)$. For the fully exclusive topology, $ep \rightarrow e\pi^+n$, the dilution factor is very high, about 0.9 on average, corresponding to the good rejection of background that is possible with the exclusivity cuts when the recoil neutron is detected. For the topology $ep \rightarrow e\pi^+(n)$, the dilution factor is reasonably good, averaging about 0.4, with some oscillations from resonance structure. At central values of $\cos(\theta^*)$, the resolution in electron-pion missing mass is poor, especially at high beam energies, causing the dilution factor to drop to 0.2 for some bins.

The dilution factors for the two π^- topologies are shown in Fig. 8 for Part 4p2o. For the fully exclusive topology, the dilution factor is quite good, averaging around 0.8. The topology with a missing proton, $ed \rightarrow e\pi^-(2p)$, has a much worse dilution factor, which is more than compensated for by a much higher event rate. The exception is at backward angles in the center of mass, where the dilution factor falls below 0.1 for the higher beam energies. In the worst cases, it is actually close to zero, implying no exclusive signal at all, compared to the very large backgrounds as $\cos(\theta^*)$ approaches -1. Asymmetry results were not evaluated for any kinematic
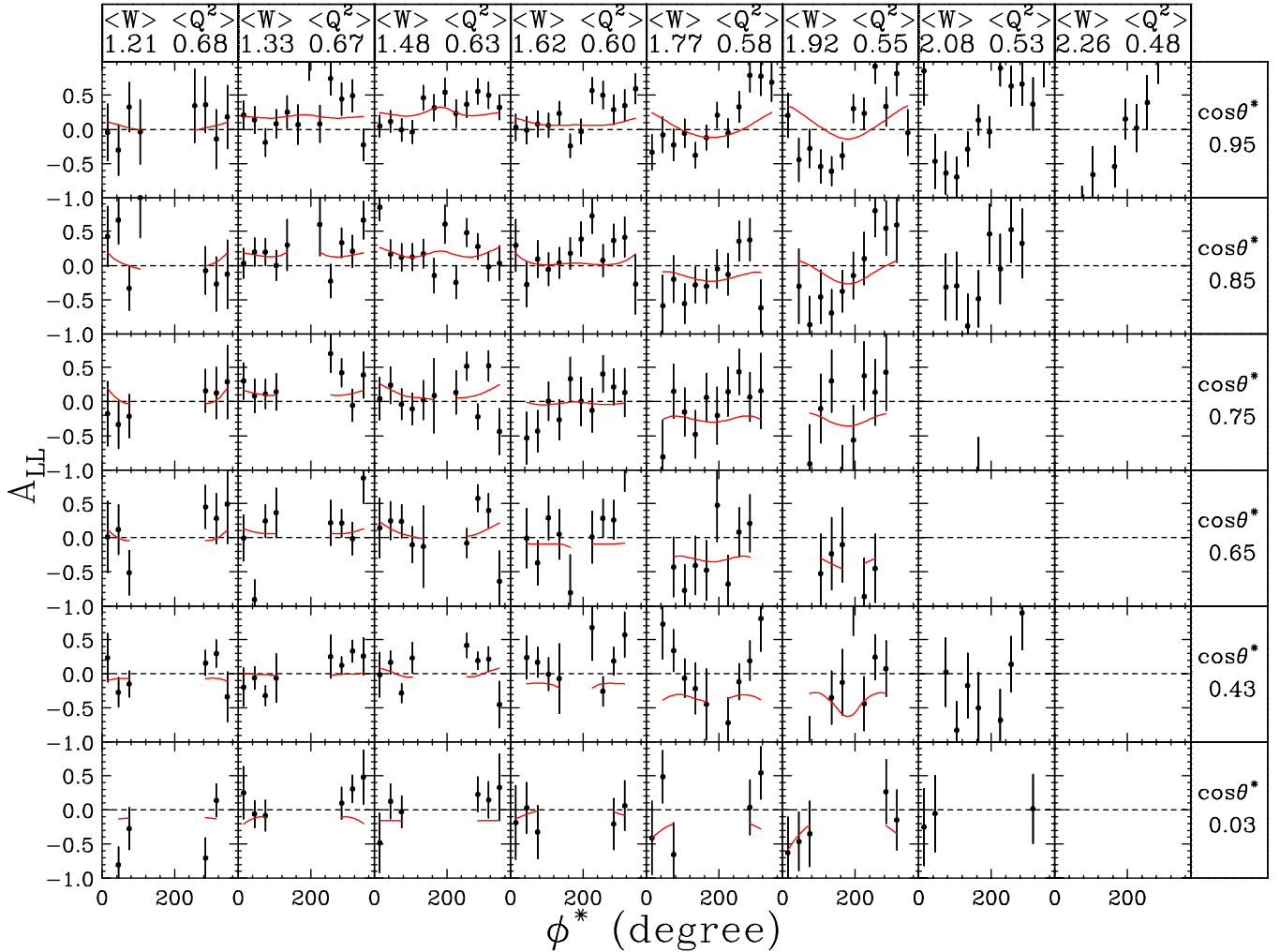
FIG. 19. Same as Fig. 17, except for a beam energy of 4.2 GeV.

bins for which the dilution factor was less than 0.1, because of the increasingly divergent uncertainty on the dilution factor.

I. Radiative corrections

An extensive study of radiative corrections to exclusive longitudinal spin asymmetries was performed using the equivalent radiator and angle-peaking approximations of the well-known Mo-Tsai formalism [29]. Although radiative corrections are very important for the extraction of cross sections, they were found to be negligible for spin asymmetries (less than 0.5%).

J. Polarized nitrogen correction

The ^{15}N isotope in the ammonia targets is slightly polarized, with a scale factor of about -0.018 relative to the free protons [30]. In the present exclusive analysis, the correction to the reaction $ep \rightarrow e\pi^+n$ is reduced to a smaller level [on average about -0.003 for topology $ep \rightarrow e\pi^+n$ and -0.009 for topology $ep \rightarrow e\pi^+(n)$] because most of the events from nitrogen are removed by the exclusivity cuts. Because of the theoretical uncertainty in evaluating the corrections, they were not applied to the data, but rather treated as a systematic

uncertainty. In the absence of D-state and final state interaction corrections, the correction to the reaction $ed \rightarrow e\pi^-p(p)$ is negligible, relative to other systematic uncertainties.

K. Combining data sets

The asymmetry analysis was performed for each topology and each part separately (see Table II). Because the in-bending and out-bending parts had similar or identical beam energies, the asymmetries should be the same in a given kinematic bin. Specifically, we combined the following parts: (1pti, 1p7o), (2p2i, 2p6i, 2p5o), (42i, 4p2o), and (5p6i, 5p72i, 5p72o). The in-bending parts favored larger scattering angles, while the out-bending parts went to much smaller electron scattering angles. Combining the two together gives a relatively uniform coverage in θ_e (and hence Q^2).

The configurations were combined by adding asymmetries together in quadrature for each of the four-dimensional bins. Because the two configurations differ only in the acceptance function, which should cancel in forming asymmetries, the expectation is that they should be fully compatible statistically. This was verified by forming the χ^2 per degree of freedom for combining each of the two asymmetries, for each of the four
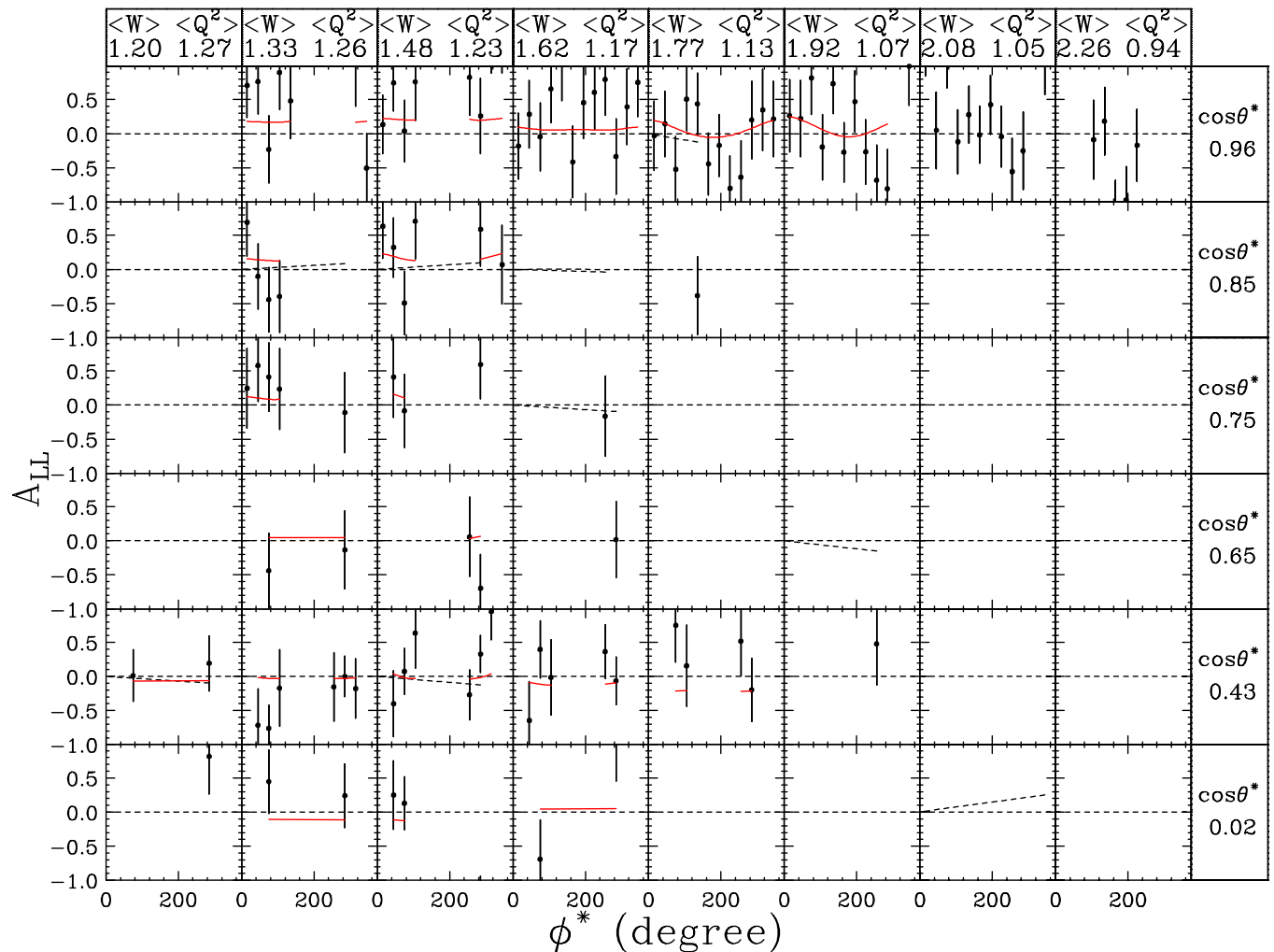
FIG. 20. Same as Fig. 17, except for a beam energy of 5.7 GeV.

topologies, and for the four beam energies. As can be seen in Table VI, the in-bending and out-bending configurations indeed are consistent with each other. The weighted average of all kinematic quantities was taken when combining the configurations.

L. Combining topologies

For both positive and negative pion electroproduction, we combined the fully exclusive topology with the one with one missing hadron. This was done by forming a weighted average of the two results on a bin-by-bin basis. For both the π^+ and π^- final states, and for both asymmetries, the topologies were found to be statistically compatible, as shown by the good values of χ^2/d.f. in Table VII. In forming χ^2, each degree of freedom corresponds to an individual point in $(W, Q^2, \cos(\theta^*), \phi^*)$ for which both topologies had at least 10 raw counts.

M. Systematic uncertainties

The systematic uncertainty in the asymmetry results is dominated by overall scale factor uncertainties arising from the uncertainties in the beam and target polarizations, and from the uncertainty in the dilution factor, as shown in Table VIII.

More details on each of the contributing factors are given in the next subsections.

1. Target and beam polarization

The product of beam and target polarization was determined for the polarized proton target from ep elastic events with a relative statistical precision ranging from 1% at low beam energies to about 3% at 5.7 GeV [21,22]. A spread of about 1.5% was observed in comparing the results with different event selection criteria. These quantities were combined in quadrature for the net uncertainty on $P_B P_T$. The relative uncertainties for the deuteron are much larger than for the proton, principally because the average target polarization is almost three times smaller for the deuteron than for the proton.

The uncertainty on the beam polarization was estimated to be 4% [21]. We combined the uncertainty on $P_B P_T$ and the uncertainty on P_B in quadrature to determine the uncertainty on P_T itself.

2. Dilution factor

The systematic uncertainty on the dilution factor arises from four factors. The first is how well the multiparameter fit describes the measured ratios of rates from the carbon and
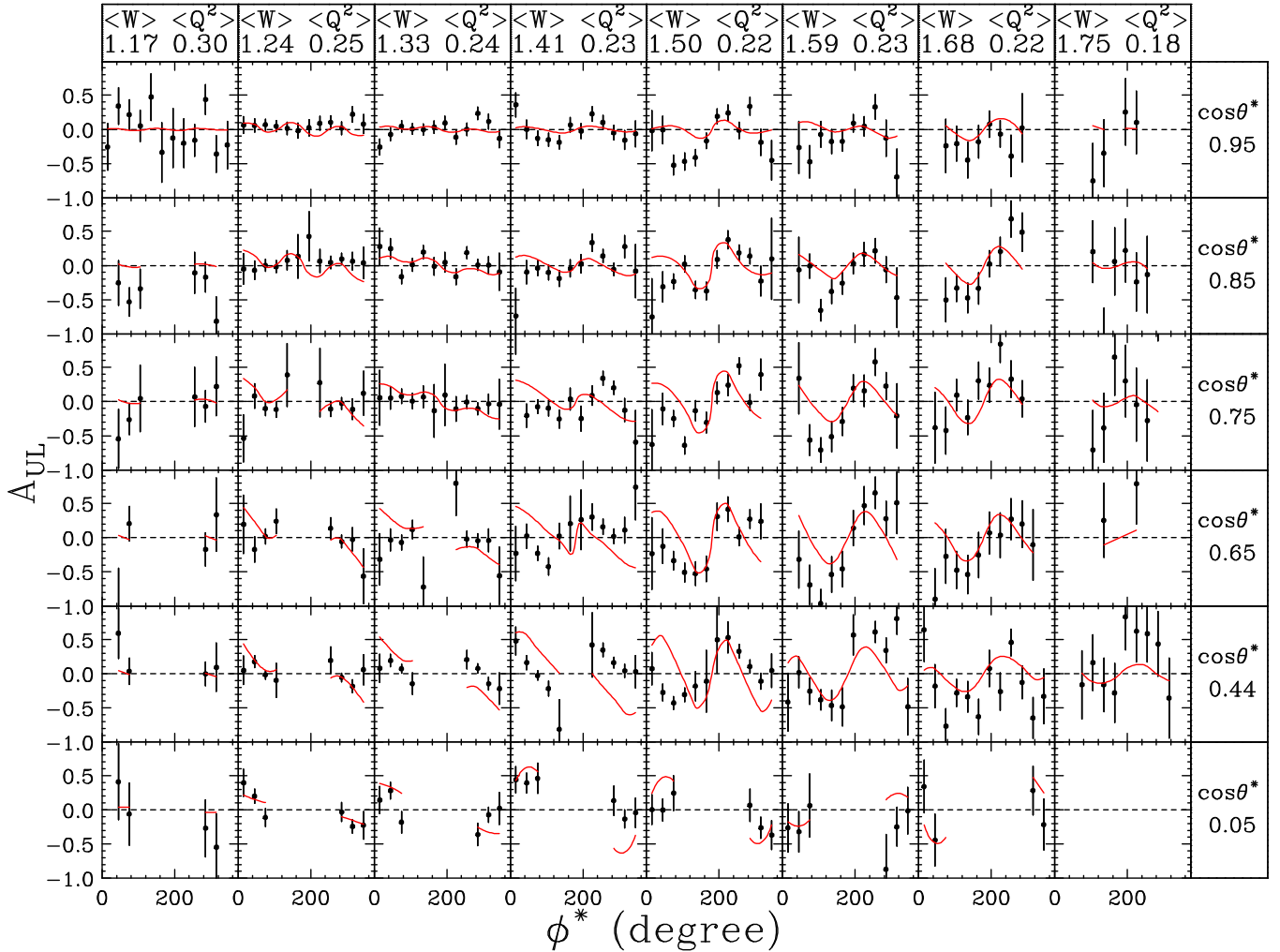
FIG. 21. Results for A_{UL} averaged over Q^2 as a function of ϕ^* in eight regions of W (left to right) and the six regions in $\cos(\theta^*)$ (top to bottom) for the reaction $ed \to e\pi^- p(p)$ and a beam energy range of 1.6–1.7 GeV. The error bars do not include systematic uncertainties. The curves are from MAID 2007. Only results with uncertainties less than 0.6 are plotted, along with the corresponding model curves. This results in some empty panels.

ammonia targets. From the reasonably good values of χ^2/d.f. for the fits, we conclude that all of the significant resonance structures in the ratios are accounted for by the fits at the few percent level. It is also possible for there to be a ϕ^* dependence to the ratios, although the fits were not improved when we included terms proportional to $\cos(\phi^*)$.

The second source of uncertainty is in the factors $R^p_{A>2}$ and $R^d_{A>2}$, defined as the ratio of protons (neutrons) in target materials with $A > 2$ for the ammonia target compared to the carbon target. We compared three methods of determining these factors: a study of inclusive electron scattering rates; fits to the electron-pion missing mass spectra for values well below the nucleon mass; and the value that gives the best agreement for A_{LL} between the fully exclusive topologies and the topologies where the recoil nucleon is not detected. This last technique relies on the fact that the fully exclusive topologies have much less nuclear background. From these comparisons, we estimate a typical systematic uncertainty of about 2% (relative) for $R^p_{A>2}$ and 4% for $R^d_{A>2}$. From Eq. (6), this translates, on average, into

approximately 4% (12%) overall normalization uncertainty on the $ep \to e\pi^+ n$ ($ed \to e\pi^- p(p)$) asymmetries A_{LL} and A_{UL}. We found the systematic uncertainty to increase with increasing beam energy, because of the limited accuracy with which the three methods could be compared at higher beam energies.

The third potential source of uncertainty comes from the fact that the carbon target contained about 20% more helium than the ammonia targets. If the ratio of helium to carbon has a significant kinematic dependence, it could translate into a variation of the dilution factor with kinematic variables, relative to the average correction. We examined the ratio of "empty target" (mostly helium) to carbon target rates within the standard cuts of the highest statistical accuracy topology, $ep \to e\pi^+(n)$, and found variations of less than $\pm 5\%$, corresponding to an uncertainty of about $\pm 1\%$ in f.

A fourth source of uncertainty could arise from a difference in the Fermi broadening in ^{15}N compared to ^{12}C, or a difference in average binding energy. To place constraints on
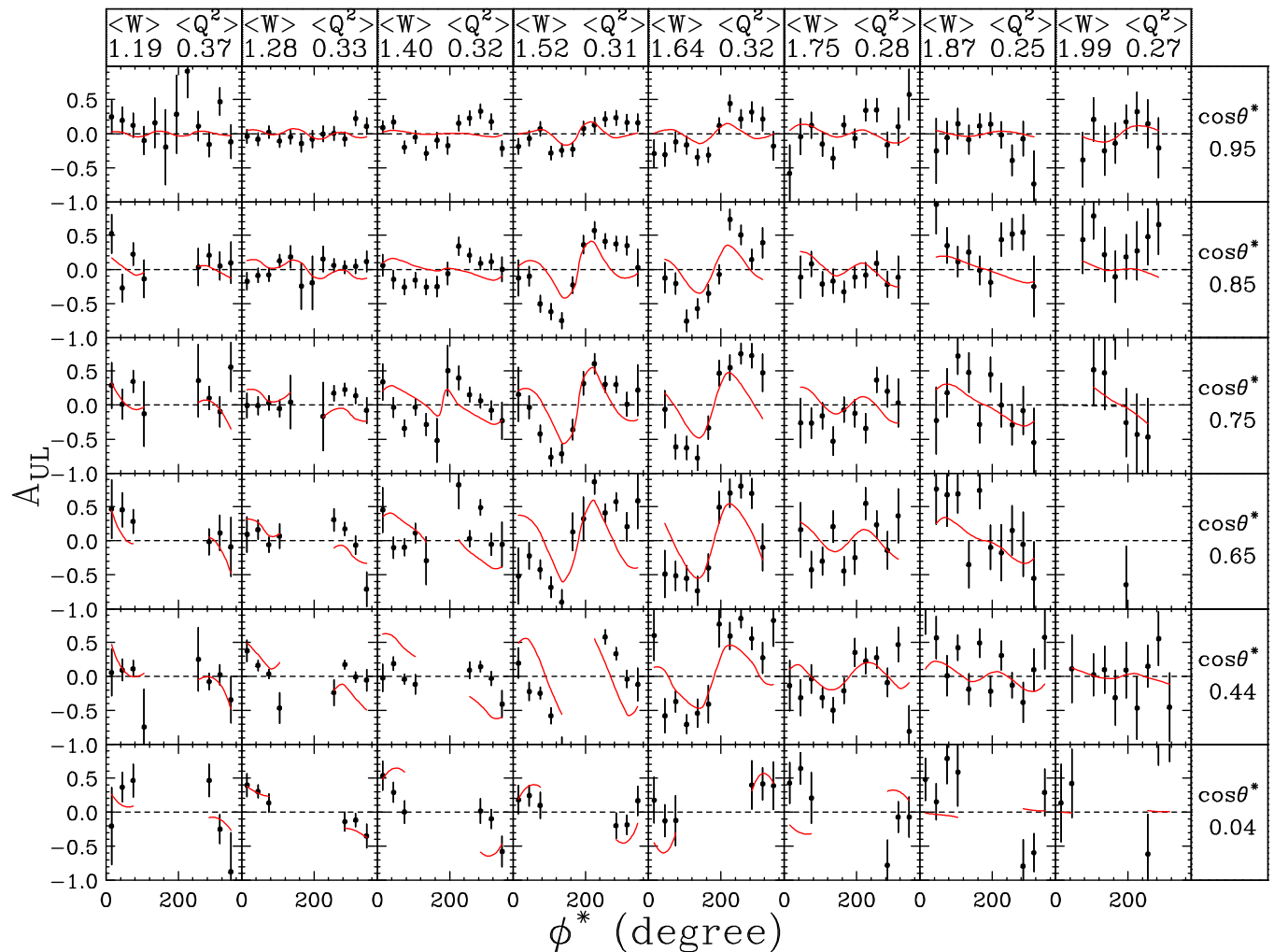
FIG. 22. Same as Fig. 21, except for a beam energy range of 2.2–2.5 GeV.

this possibility, a dedicated liquid ^{15}N target was built for the present experiment, and inclusive electron scattering rates were compared with those from carbon [28]. Within the limited statistical and systematic accuracy of the measurements (the latter being dominated by the uncertainty in the neutron-to-proton cross-section ratio), the average Fermi momentum and binding energy of the two nuclei were found to be the same.

3. Polarized nitrogen

The systematic uncertainty from the lack of a polarized nitrogen correction is estimated to be 1% for the $ep \rightarrow e\pi^+ n$ reaction [21] [assuming the one-missing-particle topology $ep \rightarrow e\pi^+(n)$ dominates] and at most 1% for the $ed \rightarrow e\pi^- p(p)$ reaction [22].

4. Multipion background

The background from multipion production was reduced to a negligible level because of a combination of two factors. First, the relatively tight cut on electron-pion missing mass, which precludes multipion background events unless the electron-proton missing mass resolution is poor (greater than

about 50 MeV). For those few kinematic bins where the resolution is this poor, the single-pion peak is so broad that the normalized nuclear background is greater than 90%. These bins were discarded by the requirement that the dilution factor be greater than 0.1. Additional constraints come from the good agreement between the fully exclusive topologies and the topologies with no recoil nucleon detected. The former has no multipion background because of the many exclusivity cuts available.

N. Asymmetries for $ep \rightarrow e\pi^+ n$ from the deuteron target

To check many aspects of the analysis of the $ed \rightarrow e\pi^- p(p)$ reaction, the $ep \rightarrow e\pi^+ n$ asymmetries from the polarized proton in the ND$_3$ target were extracted and compared to the results from the NH$_3$ target. This was done for both asymmetries and all but the highest beam energies. The same event selection and exclusivity cuts were used as for the NH$_3$ target analysis. The same values of beam and target polarization were used as for the $ed \rightarrow e\pi^- p(p)$ analysis. The dilution factor analysis used the same ratio of nucleons with $A > 2$ in the ND$_3$ target compared to the C target as the $ed \rightarrow e\pi^- p(p)$ analysis, taking into account that it is the
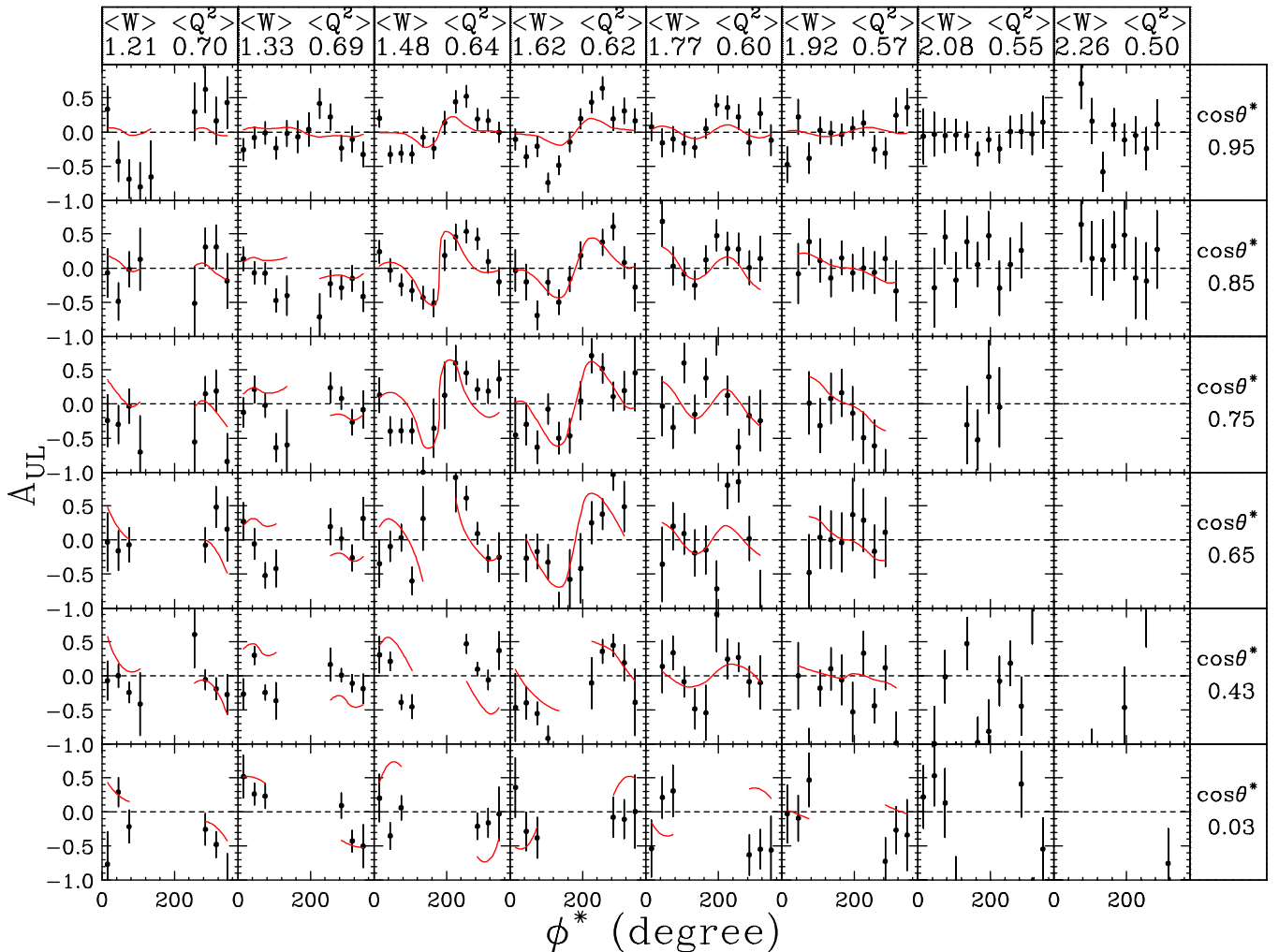
FIG. 23. Same as Fig. 21, except for a beam energy of 4.2 GeV.

number of protons that is relevant in this case, rather than the number of neutrons. A comparison of the $ep \rightarrow e\pi^+ n$ reaction from the two targets (ND_3 and ND_3) did not reveal any regions of significant differences beyond those expected from statistical fluctuations.

V. RESULTS

The results of this analysis are tabulated in two large text files, one for $ep \rightarrow e\pi^+ n$ and one for $ed \rightarrow e\pi^- p(p)$. Each line in the table contains the average value of W, Q^2, $\cos(\theta^*)$, ϕ^*, ϵ, $\cos(\phi^*)$, $\cos(2\phi^*)$, $\sin(\phi^*)$, and $\sin(2\phi^*)$ for the particular bin, as well as the two asymmetry results along with their statistical uncertainties. The systematic uncertainties are negligible in comparison on a bin-by-bin basis. Copies of the tables can be found in the CLAS data base [26] and in the Supplemental Material associated with this article [27].

With approximately 40 000 asymmetry results for $ep \rightarrow e\pi^+ n$, and 15 000 results for $ed \rightarrow e\pi^- p(p)$, it is a challenge to portray them in a compact and meaningful way. The variation with kinematic quantities was examined, and we found very little dependence on Q^2 for a given beam energy, with more significant variations as a function of W and $\cos(\theta^*)$.

There are very strong dependencies on ϕ^* for A_{UL} at all kinematic settings, as well as for A_{LL} at certain values of W and $\cos(\theta^*)$. Based on this study, the results are presented as a function of ϕ^* at each beam energy averaged over all Q^2, adjacent bin pairs in $\cos(\theta^*)$, and adjacent bin triplets in W for the $ep \rightarrow e\pi^+ n$ reaction.

A. A_{LL} for $ep \rightarrow e\pi^+ n$

The results for A_{LL} for $ep \rightarrow e\pi^+ n$ are shown in Fig. 9 (1.7 GeV beam energy), Fig. 10 (2.5 GeV), Fig. 11 (4.2 GeV), and Fig. 12 (5.7 GeV). Also shown on the plots are the results of two representative fits to previous data: the 2007 version of the MAID unitary isobar fit [15] and the unitary isobar version of the JLab Analysis of Nucleon Resonances (JANR) fit [31], averaged with the same weighting as the data points. Formally, these two fits are somewhat similar in nature, but differ in the data sets used and in the functional forms used for the Q^2 dependence of the resonance form factors. By and large, both the MAID 2007 and the JANR fits describe the data reasonably well for the lowest beam energy. At higher beam energies (and correspondingly larger values of Q^2), both fits are in reasonably good agreement with data for $W < 1.7$ GeV,
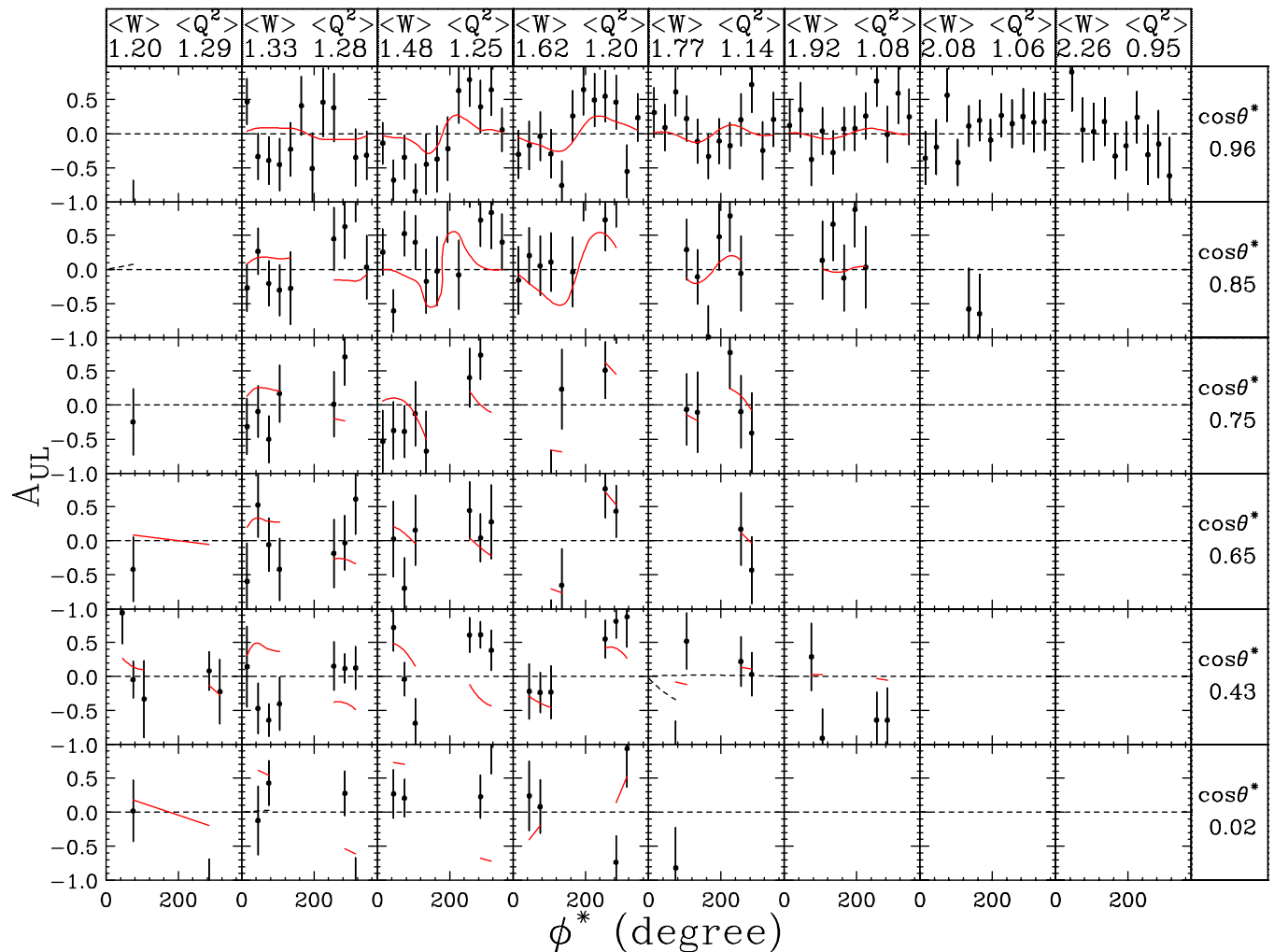
FIG. 24. Same as Fig. 21, except for a beam energy of 5.7 GeV.

but major differences can be observed at higher values of W, with the magnitude of the differences generally increasing with increasing Q^2.

B. A_{UL} for $ep \rightarrow e\pi^+n$

The results for A_{UL} for $ep \rightarrow e\pi^+n$ are shown in Fig. 13 (1.7-GeV beam energy), Fig. 14 (2.5 GeV), Fig. 15 (4.2 GeV), and Fig. 16 (5.7 GeV). Also shown on the plots are the MAID 2007 [15] and JANR [31] fits, averaged with the same weighting as the data points. By and large, MAID 2007 describes the data very well for the 1.7-GeV beam energy data, including the dramatic increase in ϕ^* dependence seen starting at $W = 1.5$ GeV. The magnitude of the ϕ^* dependence is somewhat underestimated at forward angles, however. The JANR fit also describes the data well for $W < 1.5$ GeV, with increasingly large discrepancies at higher values of W.

For the higher beam energies, both fits are in reasonable agreement with data only for $W < 1.5$ GeV. At higher values of W, disagreements generally become larger with increasing beam energy (corresponding to higher values of Q^2). In particular, the very large values of A_{UL} observed for $1.7 <$

$W < 2$ GeV and $\cos(\theta^*) < 0.8$ are not described by either fit to previous data.

C. A_{LL} for $ed \rightarrow e\pi^-p(p)$

The results for A_{LL} for $ed \rightarrow e\pi^-p(p)$ are shown in Fig. 17 (1.7-GeV beam energy), Fig. 18 (2.5 GeV), Fig. 19 (4.2 GeV), and Fig. 20 (5.7 GeV). Also shown on the plots are the results of the MAID 2007 fit [15], averaged with the same weighting as the data points. No final state corrections have been applied to the model, nor has the D-state component of the deuteron wave function been taken into account in making this comparison. The JANR fit [31] is not available for this channel. By and large, MAID 2007 describes the data moderately well although the model tends to be more negative than the data in bins where there is a difference. The largest discrepancy is for $W > 1.7$ GeV at forward angles and high Q^2, where a large difference in the ϕ^* dependence can be seen.

D. A_{UL} for $ed \rightarrow e\pi^-p(p)$

The results for A_{UL} for $ed \rightarrow e\pi^-p(p)$ are shown in Fig. 21 (1.7-GeV beam energy), Fig. 22 (2.5 GeV), Fig. 23

(4.2 GeV), and Fig. 24 (5.7 GeV). Also shown on the plots are the results of the MAID 2007 fit [15], averaged with the same weighting as the data points. In this case, the MAID fit sometimes describes the data moderately well, but in most cases where a strong ϕ^* dependence is seen in the data, it is weaker in MAID than in the data. This is particularly clear at forward angles for $1.4 < W < 1.6$ GeV: a region that is well described by MAID for the $ep \rightarrow e\pi^+ n$ reaction, but not the present $ed \rightarrow e\pi^- p(p)$ reaction.

VI. SUMMARY

Beam-target double-spin asymmetries and target single-spin asymmetries in exclusive π^+ and π^- electroproduction were obtained from scattering of 1.6, 1.7, 2.2, 2.5, 4.2, and 5.7 GeV longitudinally polarized electrons from longitudinally polarized protons and deuterons using the CLAS detector at Jefferson Lab. The kinematic range covered is $1.1 < W < 2.6$ GeV and $0.05 < Q^2 < 5$ GeV^2, greatly expanding the range of previous data. The asymmetry results are presented in large data tables which are suitable, for example, as input to the calculations of radiative corrections to semi-inclusive pion electroproduction. When used to make improved empirical fits, the data will provide powerful constraints on the Q^2 dependence of N^* and Δ^* resonance amplitudes and phases, and the interplay with nonresonant contributions. The higher W coverage compared with previous data may reveal the importance of previously poorly described nucleon resonances.

In comparison with the MAID 2007 and JANR fits, we find good agreement for the $ep \rightarrow e\pi^+ n$ asymmetries for $W < 1.7$ GeV and $Q^2 < 1$ GeV^2, a kinematic region where many data were available as input to this fit. For $W > 1.7$ GeV and higher values of Q^2, some large discrepancies with MAID are observed, particularly in the target-spin asymmetry. In the case of the $ed \rightarrow e\pi^- p(p)$ reaction, significant discrepancies with MAID are seen at all values of W, especially in A_{UL}, which is not too surprising as very few data were available prior to the present experiment to constrain fits such as MAID 2007. Clearly the new data presented in this analysis will provide powerful new constraints on global fits.

[1] C. J. Bebek *et al.*, Phys. Rev. D **13**, 25 (1976).

[2] C. J. Bebek, C. N. Brown, S. D. Holmes, R. V. Kline, F. M. Pipkin, S. Raither, L. K. Sisterson, A. Browman, K. M. Hanson, D. Larson, and A. Silverman, Phys. Rev. D **17**, 1693 (1978).

[3] T. Horn *et al.*, Phys. Rev. C **78**, 058201 (2008).

[4] H. P. Blok *et al.*, Phys. Rev. C **78**, 045202 (2008).

[5] X. Qian *et al.*, Phys. Rev. C **81**, 055209 (2010).

[6] H. Egiyan *et al.* (CLAS Collaboration), Phys. Rev. C **73**, 025204 (2006); K. Park *et al.* (CLAS Collaboration), *ibid.* **77**, 015208 (2008).

[7] K. Park *et al.* (CLAS Collaboration), Phys. Rev. C **91**, 045203 (2015).

[8] K. Park *et al.* (CLAS Collaboration), Eur. Phys. J. A **49**, 16 (2013).

[9] J. Morris *et al.*, Phys. Lett. B **73**, 495 (1978); **86**, 211 (1979).

[10] F. Foster and G. Hughes, Rep. Prog. Phys. **46**, 1445 (1983); O. Varenikova *et al.*, Z. Phys. C **37**, 251 (1988); J. Wright *et al.*, Nucl. Phys. B **181**, 403 (1981); D. Gaskell *et al.*, Phys. Rev. Lett. **87**, 202301 (2001).

[11] H. Avakian and L. Elouadrhiri, in *Proceedings High Energy Spin Physics*, edited by A. V. Efremov and O. V. Teryaev (Joint Institute for Nuclear Research, Dubna, 2003).

[12] R. De Vita *et al.* (CLAS Collaboration), Phys. Rev. Lett. **88**, 082001 (2002).

[13] X. Zheng *et al.* (CLAS Collaboration), Phys. Rev. C **94**, 045206 (2016).

[14] P. E. Bosted *et al.* (CLAS Collaboration), arXiv:1607.07518 [nucl-ex].

[15] [www.portal.kph.uni-mainz.de/MAID/]; D. Drechsel, O. Hanstein, S. S. Kamalov, and L. Tiator, Nucl. Phys. A **645**, 145 (1999).

[16] C. D. Keith *et al.*, Nucl. Instr. Meth. **501**, 327 (2003).

[17] B. A. Mecking *et al.*, Nucl. Instr. Meth. **503**, 513 (2003).

[18] Y. Prok *et al.* (CLAS Collaboration), Phys. Lett. B **672**, 12 (2009).

[19] K. V. Dharmawardane *et al.* (CLAS Collaboration), Phys. Lett. B **641**, 11 (2006).

[20] P. E. Bosted *et al.* (CLAS Collaboration), Phys. Rev. C **75**, 035203 (2007).

[21] R. G. Fersch *et al.* (CLAS Collaboration) (unpublished); R. G. Fersch, Ph.D. thesis, College of William and Mary, 2008.

[22] N. Guler *et al.* (CLAS Collaboration), Phys. Rev. C **92**, 055201 (2015).

[23] J. Pierce, Ph.D. thesis, University of Virginia, Charlottesville, 2008.

[24] S. Careccia, Ph.D. thesis, Old Dominion University, Norfolk, 2012.

[25] A. Biselli *et al.* (CLAS Collaboration), Phys. Rev. C **78**, 045204 (2008).

[26] CLAS data base [clasweb.jlab.org/physicsdb] (search for experiments eg1bexclpip and eg1bexclpim).

[27] See Supplemental Material at http://link.aps.org/supplemental/10.1103/PhysRevC.94.055201 for plain text tables of asymmetry results for the reaction $ep \rightarrow e\pi^+ n$ and plain text tables of asymmetry results for the reaction $ed \rightarrow e\pi^- p(p)$.

[28] P. E. Bosted and V. Mamyan, arXiv:1203.2262; P. E. Bosted *et al.* (CLAS Collaboration), Phys. Rev. C **78**, 015202 (2008).

[29] Y. S. Tsai, Report No. SLAC-PUB-848 (SLAC National Accelerator Laboratory, Stanford, 1971); Rev. Mod. Phys. **46**, 815 (1974).

[30] K. Abe *et al.* (SLAC E143 Collaboration), Phys. Rev. D **58**, 112003 (1998).

[31] I. G. Aznauryan, Phys. Rev. C **67**, 015209 (2003); I. G. Aznauryan *et al.* (CLAS Collaboration), *ibid.* **80**, 055203 (2009).